Attenuation by uniform suction of compressible Görtler vortices induced by free-stream vortical disturbances

Ludovico Fossà[1]† and Pierre Ricco[1]

[1]School of Mechanical, Aerospace and Civil Engineering, University of Sheffield, Sheffield S1 3JD, United Kingdom

(Received xx; revised xx; accepted xx)

Accepted in J. Fluid Mech.

The effect of uniform wall suction on compressible Görtler vortices excited by free-stream vortical disturbances is studied via asymptotic and numerical methods. The flow is described by the boundary-region framework, written and solved herein for non-similar boundary layers. The suction, applied downstream of an impermeable region, reduces the amplitude of steady and unsteady Görtler vortices. The vortices are attenuated more when the boundary layer has reached the asymptotic-suction condition than when it is streamwise-dependent. The impact of suction weakens as the free-stream Mach number increases. As the boundary layer becomes thinner, the exponential growth of the vortices is prevented because the disturbance spanwise pressure gradient and spanwise viscous diffusion are inhibited. The flow is described by the boundary-layer equations in this case, for which the wall-normal momentum equation is uninfluential at leading order and the curvature effects responsible for the inviscid pressure-centrifugal imbalance are therefore negligible. The influence of unsteadiness weakens as suction intensifies because, in the limit of a thin boundary layer, the boundary-region solution simplifies to a regular-perturbation series whose first terms are described by the steady boundary-layer equations. Suction broadens the stability regions and may favour the presence of oblique Tollmien-Schlichting waves at the expense of more energetic Görtler vortices for relatively high frequencies and moderate Mach numbers.

Key words: Boundary layer control, boundary layer receptivity, compressible boundary layers, transition to turbulence

1. Introduction

Our concern is about the convective instability that affects laminar boundary layers developing over streamwise-concave surfaces where the wall-normal pressure gradient of the disturbance cannot balance the centrifugal force. This inviscid mechanism leads to the formation of

† Present address: Complex Fluids and Flows Unit, Okinawa Institute of Science and Technology Graduate University, 1919-1 Tancha, Onna-son, Kunigami-gun, Okinawa-ken 904-0495, Japan. Email address for correspondence: ludovico-fossa@oist.jp.

Görtler vortices, streamwise-oriented and spanwise-adjacent counterrotating structures that appear when the boundary-layer thickness is comparable to their spanwise wavelength. The rapid amplification of the velocity disturbances causes the breakdown to turbulence via secondary-instability mechanisms. In compressible boundary layers, temperature fluctuations also play a role in the transition process (Wang *et al.* 2018).

The accurate computation of the generation and evolution of Görtler vortices has posed theoretical challenges. A derivation of the equations governing the linear growth of Görtler vortices in concave-plate boundary layers was given by Floryan & Saric (1979), who pointed out that the streamwise velocity component of the disturbances is asymptotically larger than the transverse components. Hall (1983) noted that the parabolic nature of these equations results in a critical dependence of the disturbance growth and neutral curves on the upstream flow conditions. In contrast to Tollmien-Schlichting (TS) waves of short streamwise wavelength, whose receptivity and growth occur in two distinct phases (Goldstein 1983), the excitation and growth of streamwise-elongated Görtler vortices take place simultaneously (Wu *et al.* 2011). In general, the computation of the vortices requires the solution of an initial-boundary-value problem where the boundary-layer disturbances match the external perturbation flow (Wu *et al.* 2011; Xu *et al.* 2024). Amongst different external flow disturbances, free-stream vortical disturbances have been recognised as powerful initiators of convective instability (Wu *et al.* 2011). Near the leading edge, the free-stream turbulence generates laminar streaks that may evolve into Görtler vortices when the wall is concave in the streamwise direction. The effect of nonlinearity on incompressible Görtler vortices generated by free-stream vortical disturbances was investigated by Xu *et al.* (2017), Marensi & Ricco (2017) and Xu *et al.* (2020) in the asymptotic framework of Leib *et al.* (1999) (henceforth LWG99). Their accurate specification of the initial and outer boundary conditions resulted in good agreement with wind tunnel data. Compressible Görtler vortices engendered by free-stream vortical disturbances were studied by Viaro & Ricco (2019*a*) and Viaro & Ricco (2019*b*). A comprehensive review of instability and transition involving compressible Görtler vortices is found in Xu *et al.* (2024).

The persistence of laminar streaks and Görtler vortices in boundary layers and their role in laminar-turbulent transition calls for methodologies aimed at their attenuation. In the compressible regime, transition delay is desirable in boundary layers over high-speed vehicles and along supersonic wind-tunnel nozzles (Xu *et al.* 2024). In the first case, this delay leads to friction drag reduction and an attenuation of the thermal surface load. In the second case, the persistence of a laminar boundary layer over nozzles is a crucial step towards the design of quiet wind tunnel sections. We are therefore motivated to investigate wall suction as a viable control strategy for compressible boundary layers over streamwise-concave surfaces.

In the following subsections, we limit the scope of the literature review to wall suction for the attenuation of laminar streaks and Görtler vortices in laminar boundary layers.

1.1. *Experimental studies*

The use of transpiration devices on wind-tunnel walls dates back to the 1960s (Schneider 2008*a*). Efforts to delay transition in supersonic wind tunnels were undertaken using longitudinal slots (Beckwith & Bertram 1972; Beckwith *et al.* 1973) and perforated plates (Leontiev & Pavlyuchenko 2008). An issue with transpiration surfaces is related to their non-uniformities and defects. These imperfections are known to generate isolated or distributed roughness effects to which the thinner suction boundary layer may be susceptible (Saric 1985; Messing & Kloker 2010). The impact of distributed roughness on high-speed transition is however still poorly understood (Schneider 2008*b*; Running *et al.* 2023). While relatively large roughness (50µm to 500µm) dramatically triggers the breakdown to turbulence in absence of suction (Bountin *et al.* 2016; Gui *et al.* 2023), Ludwieg-tube measurements at

subsonic speeds (Dimond *et al.* 2020, 2022) and experiments in incompressible wind tunnels (Methel *et al.* 2021) suggest that suction effectively delays transition even in the presence of suction holes as large as 100 µm.

Fransson & Alfredsson (2003) applied uniform suction through a sintered-plastic plate with small pores ($\cong$ 10 µm) and reported an attenuation of TS waves and laminar streaks at low speeds and high free-stream turbulence levels. Their results show a gradual evolution of the Blasius boundary layer to the asymptotic-suction boundary layer (ASBL) over the porous plate. Despite a twofold reduction in the boundary-layer thickness, the spanwise wavelength of the streaks λ_z^* was not affected. Yoshioka *et al.* (2004) measured λ_z^* in a series of experiments with suction, concluding that its value was primarily determined by the shape of the leading edge and the oncoming free-stream perturbation flow. Kurian & Fransson (2011) investigated the evolution of disturbances induced in an ASBL by an array of roughness elements. Their findings showed good agreement with optimal growth predictions when the optimization time was chosen to fit the experimental data.

The experimental studies on the influence of suction on Görtler vortices are very limited. Mangalam *et al.* (1987) placed spanwise-aligned rods on the concave section of a wing profile and reported an attenuation of the velocity fluctuations associated with Görtler vortices. A selective transpiration technique was employed by Myose & Blackwelder (1995) on a concave boundary layer. They applied suction at periodic spanwise locations where the low-speed streaks were known to develop and reported a delay in the breakdown of the Görtler vortices.

To the best of the authors' knowledge, there are no experimental investigations on compressible Görtler vortices evolving in suction boundary layers. Li *et al.* (2018) examined the use of uniform suction to mitigate Görtler instability on flared cones at zero angle of attack in a hypersonic wind tunnel. To that end, they manufactured a model comprising an aft cone and a rear flared cone with a truncated permeable volume installed on the aft section, although no measurements of the perturbed flow in the boundary layer were conducted. Furthermore, wall suction has never been used to attenuate Görtler vortices in boundary layers along the nozzles of supersonic wind tunnels, over the external wetted surfaces of aircraft or over the internal surfaces of aircraft engine intakes. Suction actuators have successfully delayed transition in boundary layers on aircraft wings, yet with no evidence that the perturbations involved were Görtler vortices (Krishnan *et al.* 2017).

1.2. *Studies based on direct numerical simulations*

Sescu *et al.* (2018) and Sescu *et al.* (2019) investigated the effect of localised blowing and suction by performing direct numerical simulations of a supersonic concave boundary layer. They implemented a feedback control algorithm to attenuate the nonlinear growth of the vortices. Direct numerical simulations were also employed to study how wall transpiration modifies perturbed Mach-6 boundary layers over flared cones, by Hader & Fasel (2021) for the case of alternate blowing and suction and by Hollender *et al.* (2019) for the case of distributed suction, with the objective to reproduce the flow configuration studied experimentally by Li *et al.* (2018).

1.3. *Theoretical studies*

The effect of uniform wall transpiration on the linear stability of Görtler vortices has been studied for self-similar and asymptotic suction (Kobayashi 1972, 1974; El-Hady & Verma 1981, 1984; Floryan & Saric 1983). Self-similar suction, which features an unbounded wall-normal velocity as the leading edge is approached, has never been implemented in laboratory. Self-similar solutions offer the advantage of being more tractable theoretically and often provide valuable insights into stability and transition, especially when solving a

system of partial differential equations is not feasible (Stewartson 1964; Anderson 2019; Al-Malki *et al.* 2021). Ricco & Dilib (2010) and Ricco *et al.* (2013) imposed self-similar suction on incompressible and compressible laminar base flows to study the receptivity and growth of streaks and oblique TS waves within the asymptotic framework of Ricco & Wu (2007) and LWG99. Marensi & Ricco (2017) solved the nonlinear boundary-region equations in the asymptotic framework of LWG99 and reported a marked attenuation of the Görtler vortices in the presence of spanwise-dependent wall suction. Es-Sahli *et al.* (2023) applied an optimal-control technique to the nonlinear boundary-region equations and reported a marked attenuation of the energy growth. Within these theoretical frameworks, uniform wall suction has never been utilised to attenuate the growth of Görtler vortices at any Mach number.

The laminar flow modified by uniform suction is initially streamwise-dependent, the asymptotic-suction solution being valid only sufficiently downstream of the suction onset. This solution was derived for the first time by Griffith & Meredith (1936) and extended to the compressible regime by Young (1948). Morduchow (1963) showed that the ASBL solution remains valid in the presence of streamwise pressure gradients. An exact compressible solution was derived by Lew & Fanucci (1955) for the case where the wall suction was uniform at any streamwise location, while Görtler (1957) treated the case of arbitrary distributions of the suction velocity in the incompressible regime.

1.4. *Outline of the study*

We aim to study the growth of compressible Görtler vortices developing on a concave wall with steady uniform suction applied downstream of an impermeable region. The receptivity of the base flow to external perturbations is a central ingredient of our framework, i.e. the Görtler vortices are generated by – and continuously exposed to – free-stream vortical disturbances. Our analysis is concerned with the flow configurations and disturbance wavelengths commonly reported in the experimental literature (e.g. Ciolkosz & Spina 2006; Wang *et al.* 2018; Li *et al.* 2018; de Luca *et al.* 1993). The theoretical framework of LWG99, adapted by Wu *et al.* (2011) and Viaro & Ricco (2019*a*) to the case of self-similar boundary layers over concave walls, is thus extended to and solved for non-similar compressible boundary layers for the first time.

We shall consider the case where uniform suction is applied downstream of an impermeable region. The velocity and temperature distributions of the laminar base flow do not obey self-similarity and the evolution of the laminar flow must be described by the non-similar boundary-layer equations (e.g. Cebeci 2002), as shown by Fransson & Alfredsson (2003) in the incompressible case. Furthermore, the receptivity of the base flow to free-stream vortical disturbances plays a critical role in the vicinity of the leading edge where the suction velocity is zero or finite. This effect is another compelling reason why neither the self-similar suction model nor the ASBL model can provide an accurate description of the base flow of interest herein.

The asymptotic framework, the governing equations of the base flow and the disturbance flow, and the boundary conditions are discussed in §2. The validation of the non-similar laminar base flow, the effect of suction on the growth of the compressible Görtler vortices and the behaviour of the neutral stability curves are discussed in §3. Conclusions are drawn in §4.

2. Mathematical formulation

As shown in figure 1, we consider a uniform flow of velocity U^*_∞ and temperature T^*_∞ past a thin concave plate with radius of curvature r^*_c. This flow generates a thin boundary layer

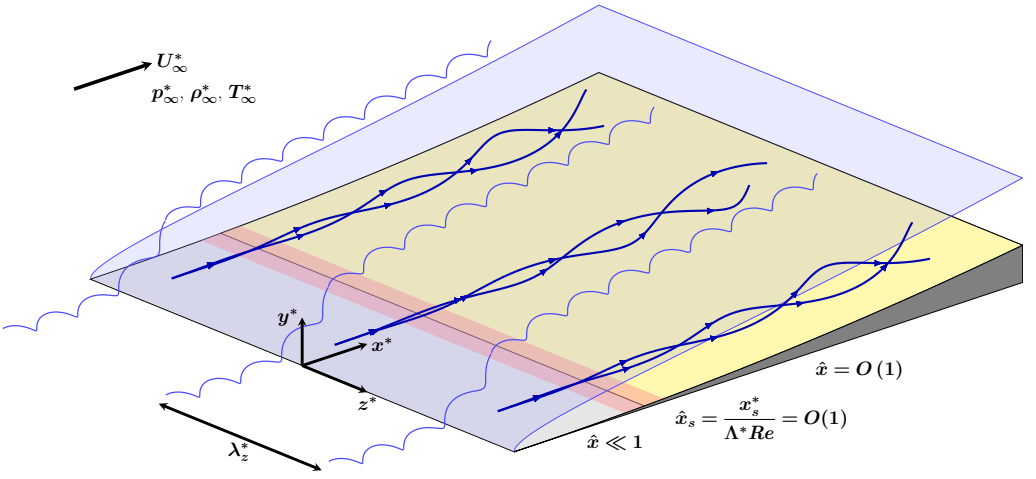

Figure 1: Schematic of the flow system. Görtler vortices grow over a concave plate under the continuous forcing of free-stream vorticity. The plate is infinitely thin at the leading edge and uniform suction is applied in the yellow region $\hat{x} > \hat{x}_s$. The disturbance flow is periodic along the spanwise (z^*) direction and the plate has an infinite spanwise width.

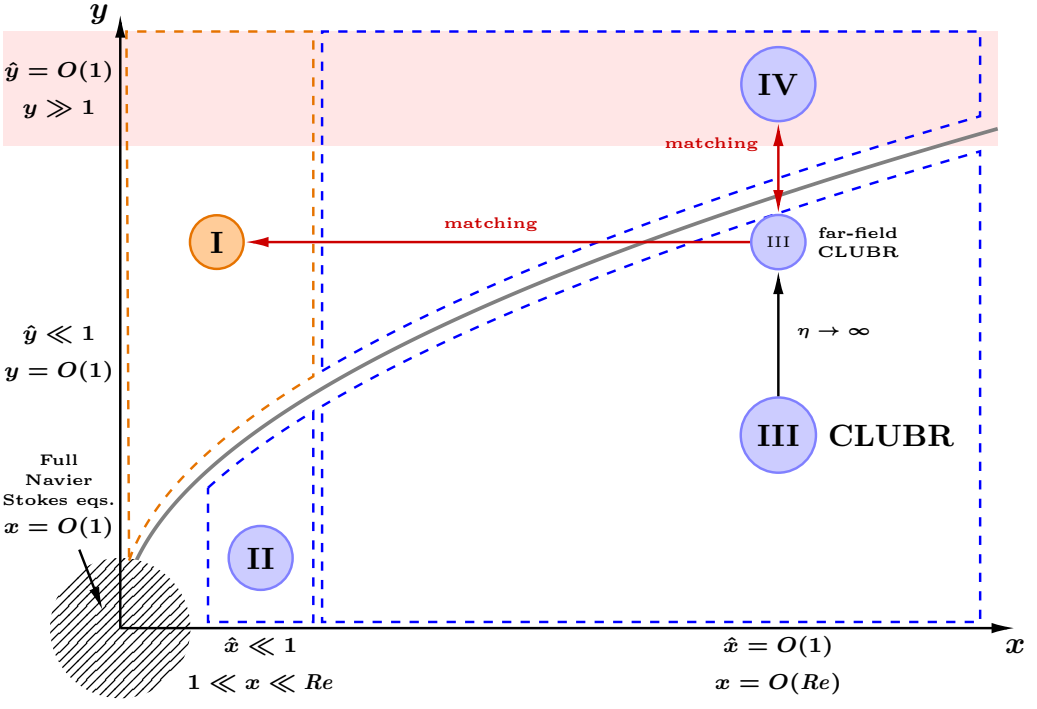

Figure 2: Schematic of the four asymptotic regions introduced by LWG99 and their domains (dashed lines). The disturbance flow is inviscid in region I (orange) and viscous in regions II, III, and IV (blue). The boundary layer thickness is shown in gray. The laminar streaks and the Görtler vortices develop in region III, where the flow is governed by the CLUBR equations introduced in §2.2. The solution to the far-field ($\eta \gg 1$) form of the CLUBR equations matches the inviscid flow in region I (2.1) for $\hat{x} \to 0$ and the inner limit of region IV ($\hat{y} \to 0$) for large $y \to \infty$. The size of the regions is not to scale.

of thickness $\delta^* \ll r_c^*$ over the plate. Wall suction is applied by imposing a streamwise-dependent wall-normal velocity V_w at the wall. Downstream of an impermeable region (gray area in figure 1) followed by a thin adjustment region centred at x_s^* (red area in figure 1), the wall suction velocity is uniform (yellow area in figure 1). The flow is described in a curvilinear, orthogonal system of coordinates $\{x^*, y^*, z^*\}$ centred at the leading edge. The streamwise coordinate x^* follows the curvature of the plate, and y^* and z^* denote the wall-normal and spanwise coordinates, respectively. The flow is spanwise-periodic and the concave plate has an infinite spanwise width. All dimensional quantities are denoted by the superscript $*$. The governing equations are derived by introducing the Lamé coefficients $\left\{1 - y^*/r_c^*, 1, 1\right\}$ in the Navier-Stokes equations (e.g. El-Hady & Verma 1984; Viaro & Ricco 2019*a*). The spatial lengths are normalised using $\Lambda^* = \lambda_z^*/2\pi$, where λ_z^* denotes the spanwise wavelength of the disturbances (LWG99). Unlike the boundary-layer thickness, λ_z^* remains constant in both the free-stream and in the boundary layer, regardless of whether suction is applied or not (Tani 1962; Finnis & Brown 1997; Fransson & Alfredsson 2003; Yoshioka *et al.* 2004; Tandiono *et al.* 2008). Furthermore, laminar streaks and Görtler vortices emerge at downstream locations where the boundary-layer thickness has grown to a magnitude comparable to λ_z^*, making λ_z^* the natural length scale of the problem (Swearingen & Blackwelder 1987; Matsubara & Alfredsson 2001; Wu *et al.* 2011). The velocity components $\{u^*, v^*, w^*\}$, the density ρ^* and the temperature T^* scale with their reference free-stream values, U_∞^*, ρ_∞^* and T_∞^*. The pressure is normalised by $\rho_\infty^* U_\infty^{*2}$ and the time is scaled by Λ^*/U_∞^*. The Reynolds number is $Re = \rho_\infty^* U_\infty^* \Lambda^*/\mu_\infty^* \gg 1$, while the Mach number $Ma = U_\infty^*/\left(\gamma \mathcal{R}^* T_\infty^*\right)^{1/2} = O(1)$, where μ^* is the dynamic viscosity, $\gamma = 1.4$ is the heat capacity ratio and $\mathcal{R}^* = 287.05\,\mathrm{J\,kg^{-1}\,K^{-1}}$ is the perfect gas constant of air. The Prandtl number is $Pr = \gamma\,(\gamma - 1)^{-1}\,\mu_\infty^* \mathcal{R}^*/k_\infty^* = 0.71$, where k^* is the thermal conductivity. Scaled quantities are not indicated by any symbol.

We follow the receptivity framework first introduced in LWG99. The framework relies on the assumption of large-Re flows and streamwise-elongated, spanwise-periodic disturbances with a small streamwise wavenumber $k_x \ll 1$. It is convenient to introduce the scaled variables $\hat{x} = x/Re$ and $\hat{t} = t/Re$. A distinguished scaling emerges and the domain splits in the four asymptotic regions shown in figure 2. Region I and II are near the leading edge, at $\hat{x} \ll 1$ (but $1 \ll x \ll Re$), where the boundary-layer thickness is smaller than the spanwise wavelength of the disturbance, i.e. $\delta = \delta^*/\Lambda^* \ll 1$. The viscous effects are confined in this thin boundary layer in region II, where the disturbance flow is governed by the unsteady boundary-layer equations. Small-amplitude, non-interacting vortical disturbances are passively advected by the inviscid flow in region I, where $y = O(1)$. They take the form of monochromatic perturbations of the gust type,

$$\boldsymbol{u} - \boldsymbol{i} = \epsilon \hat{\boldsymbol{u}}^\infty \mathrm{e}^{\mathrm{i}\left(\boldsymbol{k}\cdot\boldsymbol{x} - \mathcal{F}\hat{t}\right)} + \text{c.c.}, \tag{2.1}$$

where $\epsilon \ll 1$, $\hat{\boldsymbol{u}}^\infty = \{\hat{u}^\infty, v^\infty, \hat{w}^\infty\}$ is the gust amplitude, $\boldsymbol{k} = \left\{k_x, k_y, k_z\right\}$ is the wavenumber vector, $\boldsymbol{i}$ is the streamwise (x^*) versor and c.c. indicates the complex conjugate. The parameter $\mathcal{F} = k_x Re = \rho_\infty^* 2\pi f^* \Lambda^{*2}/\mu_\infty^* = O(1)$ is the scaled disturbance frequency f^*.

Region III and IV are located further downstream at $\hat{x} = O(1)$. There, $\delta^*/\Lambda^* = O(1)$, the spanwise and wall-normal viscous diffusion are comparable and low-frequency, streamwise-elongated gusts induce three-dimensional disturbances within the boundary layer. Viscous effects are confined within the thicker boundary layer in region III, where $y = O(1)$ and the laminar streaks and the Görtler vortices ensue. The evolution of these structures is governed by the unsteady boundary-region equations, which represent the rigorous asymptotic limit of the Navier-Stokes equations for $k_x \ll 1$ and $Re \gg 1$. The large disparity between spanwise and streamwise scales results in $O(\epsilon)$ free-stream fluctuations generating $O(\epsilon Re)$ streamwise

velocity disturbances in region III. The inviscid outer flow is influenced by the boundary-layer displacement in region IV, where $y = O(Re)$ and the gusts (2.1) decay as they are advected downstream.

For asymptotically small disturbance amplitude $r_t = \epsilon Re \ll 1$, the unsteady, three-dimensional disturbance flow $\grave{\boldsymbol{q}}$ is linearised about the steady, two-dimensional laminar base flow $\boldsymbol{Q}$, i.e. $\boldsymbol{q}\left(\hat{x}, y, z, \hat{t}\right) = \boldsymbol{Q}\left(\hat{x}, y\right) + \epsilon\grave{\boldsymbol{q}}\left(\hat{x}, y, z, \hat{t}\right)$:

$$\{u, v, w, \tau, p\}\left(\hat{x}, y, z, \hat{t}\right) = \left\{U, V, 0, T, \frac{1}{\gamma Ma^2}\right\}\left(\hat{x}, y\right) + \epsilon\left\{\grave{u}, \grave{v}, \grave{w}, \grave{\tau}, \grave{p}\right\}\left(\hat{x}, y, z, \hat{t}\right). \quad (2.2)$$

In our case of uniform suction downstream of an impermeable region, the base flow $\boldsymbol{Q}$ is not self-similar. It is governed by a system of parabolic partial differential equations, the compressible Blasius solution being valid only along the impermeable region $\hat{x} < \hat{x}_s$.

2.1. *The non-similar laminar base flow*

We now obtain the non-similar, compressible boundary-layer equations with emphasis on the derivation of the wall-normal velocity component V. To the best of the authors' knowledge, this derivation is not available in the literature. We first define a streamfunction $\psi\left(\hat{x}, y\right)$ that satisfies the continuity equation $\rho U = \partial\psi/\partial y$ and $\rho V = -Re^{-1}\partial\psi/\partial\hat{x}$. The governing equations are derived in terms of the normalised streamfunction $F\left(\hat{x}, \eta\right) = \psi\left(\hat{x}, y\right)\left(2\hat{x}\right)^{-1/2}$ and the similarity variable $\eta(\hat{x}, y) = \bar{Y}(\hat{x}, y)\left(2\hat{x}\right)^{-1/2}$, where

$$\bar{Y}\left(\hat{x}, y\right) \equiv \int_0^y \left[T\left(\hat{x}, \breve{y}\right)\right]^{-1} \mathrm{d}\breve{y} \quad (2.3)$$

is the Dorodnitsyn-Howarth variable (Stewartson 1964). Inverting (2.3) yields

$$y\left(\hat{x}, \eta\right) = \left(2\hat{x}\right)^{1/2} \int_0^\eta T\left(\hat{x}, \breve{\eta}\right) \mathrm{d}\breve{\eta}. \quad (2.4)$$

The use of η is convenient because the boundary layer is self-similar along the impermeable region and because the initial and outer boundary conditions are more readily specified in terms of η (Xu *et al.* 2020). The streamwise momentum and static-enthalpy balance equations that govern the base flow $\boldsymbol{Q}$ are (e.g. Cebeci 2002)

$$\left(\frac{\mu}{T}F''\right)' + FF'' = 2\hat{x}\left(F'\left.\frac{\partial F'}{\partial\hat{x}}\right|_\eta - F''\left.\frac{\partial F}{\partial\hat{x}}\right|_\eta\right), \quad (2.5a)$$

$$FT' + (\gamma - 1)\,Ma^2\frac{\mu}{T}\left(F''\right)^2 + \frac{1}{Pr}\left(\frac{\mu}{T}T'\right)' = 2\hat{x}\left(F'\left.\frac{\partial T}{\partial\hat{x}}\right|_\eta - T'\left.\frac{\partial F}{\partial\hat{x}}\right|_\eta\right), \quad (2.5b)$$

where the prime denotes differentiation in η and the viscosity μ is modelled with Sutherland's law. The wall-normal velocity component of the base flow V (2.2) is found by applying the chain rule to $\partial\psi/\partial\hat{x}$ and introducing the perfect gas equation $\rho T = 1$

$$V\left(\hat{x}, \eta\right) = -\frac{T}{Re}\frac{\partial\psi}{\partial\hat{x}} = -\frac{1}{Re\left(2\hat{x}\right)^{1/2}}\left(TF + 2\hat{x}T\left.\frac{\partial F}{\partial\hat{x}}\right|_\eta + 2\hat{x}T\left.\frac{\partial\eta}{\partial\hat{x}}\right|_y F'\right). \quad (2.6)$$

The unknown term $\partial\eta/\partial\hat{x}|_y$ is found by recalling that $\hat{x}$ and y are orthogonal, and thus the total derivative of (2.4) with respect to $\hat{x}$ is null. Using the chain rule yields

$$\frac{\partial y\left(\hat{x}, \eta\right)}{\partial\hat{x}} = \left.\frac{\partial y\left(\hat{x}, \eta\right)}{\partial\hat{x}}\right|_\eta + \left.\frac{\partial\eta\left(\hat{x}, y\right)}{\partial\hat{x}}\right|_y \left.\frac{\partial y\left(\hat{x}, \eta\right)}{\partial\eta}\right|_{\hat{x}} = 0, \quad (2.7)$$

where

$$\left.\frac{\partial y\left(\hat{x},\eta\right)}{\partial\hat{x}}\right|_{\eta}=\frac{1}{\left(2\hat{x}\right)^{1/2}}\int_{0}^{\eta}T\left(\hat{x},\check{\eta}\right)\mathrm{d}\check{\eta}+\left(2\hat{x}\right)^{1/2}\int_{0}^{\eta}\left.\frac{\partial T}{\partial\hat{x}}\right|_{\eta}\mathrm{d}\check{\eta},\tag{2.8a}$$

$$\left.\frac{\partial y\left(\hat{x},\eta\right)}{\partial\eta}\right|_{\hat{x}}=\left(2\hat{x}\right)^{1/2}T\left(\hat{x},\eta\right).\tag{2.8b}$$

The derivative (2.8*a*) represents the rate of change in y due to a change in $\hat{x}$ while moving along a path at fixed η. The derivative (2.8*b*) is the rate of change in y due to a variation in η while $\hat{x}$ is fixed. The sought derivative $\left.\partial\eta/\partial\hat{x}\right|_{y}=-\left.\partial y/\partial\hat{x}\right|_{\eta}\left(\left.\partial y/\partial\eta\right|_{\hat{x}}\right)^{-1}$ is

$$\left.\frac{\partial\eta\left(\hat{x},y\right)}{\partial\hat{x}}\right|_{y}=-\frac{1}{2\hat{x}T\left(\hat{x},\eta\right)}\int_{0}^{\eta}T\left(\hat{x},\check{\eta}\right)\mathrm{d}\check{\eta}-\frac{1}{T\left(\hat{x},\eta\right)}\int_{0}^{\eta}\left.\frac{\partial T}{\partial\hat{x}}\right|_{\check{\eta}}\mathrm{d}\check{\eta}\equiv-\frac{\eta_{c}}{2\hat{x}},\tag{2.9}$$

where the compressible similarity variable $\eta_{c}\left(\hat{x},\eta\right)$

$$\eta_{c}\left(\hat{x},\eta\right)\equiv\frac{1}{T\left(\hat{x},\eta\right)}\int_{0}^{\eta}\left[T\left(\hat{x},\check{\eta}\right)+2\hat{x}\left.\frac{\partial T}{\partial\hat{x}}\right|_{\check{\eta}}\right]\mathrm{d}\check{\eta},\tag{2.10}$$

is defined. Equation (2.10) reduces to $\eta_{c}(\eta)=T^{-1}\int_{0}^{\eta}T\mathrm{d}\check{\eta}$ in the self-similar case (Viaro & Ricco 2019*a*). The self-similar form of (2.10) can also be derived by expanding the integral in (3.1.5) in Stewartson (1964, p. 36).

The base-flow velocity components

$$U\left(\hat{x},\eta\right)=F',\tag{2.11a}$$

$$V\left(\hat{x},\eta\right)=\frac{T}{Re\left(2\hat{x}\right)^{1/2}}\left(\eta_{c}F'-F-2\hat{x}\left.\frac{\partial F}{\partial\hat{x}}\right|_{\eta}\right),\tag{2.11b}$$

reduce to (2.7a,b) in Viaro & Ricco (2019*a*) in the self-similar case. The wall is adiabatic, $T'\left(\hat{x},0\right)=0$. A no-slip condition is imposed on the streamwise velocity component, $F'\left(\hat{x},0\right)=0$, while the effect of the transpiration velocity $V_{w}=V\left(\hat{x},0\right)$ is described by the equation

$$\left[F+2\hat{x}\left.\frac{\partial F}{\partial\hat{x}}\right|_{\eta}+\frac{\gamma_{w}\left(2\hat{x}\right)^{1/2}}{T}\right]\left(\hat{x},0\right)=0,\tag{2.12}$$

where $\gamma_{w}\left(\hat{x}\right)=V_{w}Re=O(1)$ is the suction parameter. We use the incompressible definition of γ_{w} (Floryan & Saric 1983) rather than the compressible one (El-Hady & Verma 1984) because $T\left(\hat{x},0\right)$ is not constant. The non-dimensional suction velocity $V_{w}\ll1$ is also known as the suction coefficient in the experimental literature (e.g. Myose & Blackwelder 1995; Fransson & Alfredsson 2003; Leontiev & Pavlyuchenko 2008) and typically ranges between 10^{-5} and 10^{-3}. The velocity and the temperature are uniform in the external region, i.e. $F'\rightarrow1$ and $T\rightarrow1$ for $\eta\gg1$.

In the limit of large streamwise distance, the two-dimensional steady boundary-layer equations tend to the compressible asymptotic-suction (ASBL) system of ordinary differential equations (Young 1948; Morduchow 1963),

$$\frac{\mathrm{d}}{\mathrm{d}N}\left(\frac{\mu}{T}\frac{\mathrm{d}U}{\mathrm{d}N}+U\right)=0,\tag{2.13a}$$

$$\frac{1}{Pr}\frac{\mathrm{d}}{\mathrm{d}N}\left(\frac{k}{T}\frac{\mathrm{d}T}{\mathrm{d}N}+T\right)+\left(\gamma-1\right)Ma^{2}\frac{\mu}{T}\left(\frac{\mathrm{d}U}{\mathrm{d}N}\right)^{2}=0,\tag{2.13b}$$

where $N = -\gamma_w \bar{Y}/T_w$, $\bar{Y}$ is defined in (2.3) and T_w is the wall temperature.

2.2. *The unsteady, three-dimensional disturbance flow*

The disturbance flow $\grave{\boldsymbol{q}}$ in region III is governed by the compressible linearised unsteady boundary-region equations (CLUBR). By substituting the expansion (2.2) with the disturbances (Floryan & Saric 1979; Leib *et al.* 1999; Wu *et al.* 2011)

$$\grave{\boldsymbol{q}} = \mathrm{i}k_z \check{w} Re \left\{ \bar{u}, \frac{(2\hat{x})^{1/2}}{Re}\bar{v}, \frac{\bar{w}}{\mathrm{i}k_z Re}, \bar{\tau}, \frac{\bar{p}}{Re^2} \right\} \mathrm{e}^{\mathrm{i}(k_z z - \mathcal{F}\hat{t})} \tag{2.14}$$

– where $\check{w} = \hat{w}^\infty + \mathrm{i}k_z \hat{v}^\infty / \left(k_x^2 + k_z^2\right)^{1/2} = O(1)$ – into the compressible Navier-Stokes equations, and by assuming $r_c = r_c^*/\Lambda^* = O(Re^2)$, the CLUBR continuity $\mathcal{C}$, streamwise momentum $\mathcal{X}$, wall-normal momentum $\mathcal{Y}$, spanwise momentum $\mathcal{Z}$ and enthalpy $\mathcal{E}$ balances are recovered

$$\begin{aligned}
\mathcal{C}| \; & \left(\frac{\eta_c T'}{2\hat{x}T} - \frac{1}{T}\left.\frac{\partial T}{\partial \hat{x}}\right|_\eta \right) \bar{u} + \left.\frac{\partial \bar{u}}{\partial \hat{x}}\right|_\eta - \frac{\eta_c}{2\hat{x}}\frac{\partial \bar{u}}{\partial \eta} - \frac{T'}{T^2}\bar{v} + \frac{1}{T}\frac{\partial \bar{v}}{\partial \eta} + \bar{w} + \left(\frac{\mathrm{i}\mathcal{F}}{T} + \right. \\
& \left. + \frac{F'}{T^2}\left.\frac{\partial T}{\partial \hat{x}}\right|_\eta - \frac{T'}{T^2}\left.\frac{\partial F}{\partial \hat{x}}\right|_\eta - \frac{FT'}{2\hat{x}T^2} \right) \bar{\tau} - \frac{F'}{T}\left.\frac{\partial \bar{\tau}}{\partial \hat{x}}\right|_\eta + \left(\frac{F}{2\hat{x}T} + \frac{1}{T}\left.\frac{\partial F}{\partial \hat{x}}\right|_\eta \right) \frac{\partial \bar{\tau}}{\partial \eta} = 0, \qquad (2.15a)
\end{aligned}$$

$$\begin{aligned}
\mathcal{X}| \; & \left(k_z^2 \mu T - \mathrm{i}\mathcal{F} - \frac{\eta_c F''}{2\hat{x}} + \left.\frac{\partial F'}{\partial \hat{x}}\right|_\eta \right) \bar{u} + F' \left.\frac{\partial \bar{u}}{\partial \hat{x}}\right|_\eta - \left(\frac{F}{2\hat{x}} + \left.\frac{\partial F}{\partial \hat{x}}\right|_\eta \right) \frac{\partial \bar{u}}{\partial \eta} + \\
& + \frac{1}{2\hat{x}} \left(\frac{\mu}{T}\frac{\partial \bar{u}}{\partial \eta} \right)' + \frac{F''}{T}\bar{v} + \left(\frac{FF''}{2\hat{x}T} - \frac{F'}{T}\left.\frac{\partial F'}{\partial \hat{x}}\right|_\eta + \frac{F''}{T}\left.\frac{\partial F}{\partial \hat{x}}\right|_\eta \right) \bar{\tau} - \left(\frac{\mu' F''}{2\hat{x}T}\bar{\tau} \right)' = 0, \qquad (2.15b)
\end{aligned}$$

$$\begin{aligned}
\mathcal{Y}| \; & \left(\frac{TF - \eta_c TF' + \eta_c T' F - \eta_c^2 TF''}{4\hat{x}^2} - \left.\frac{\partial T}{\partial \hat{x}}\right|_\eta \left.\frac{\partial F}{\partial \hat{x}}\right|_\eta - T\left.\frac{\partial^2 F}{\partial \hat{x}^2}\right|_\eta - \frac{F}{2\hat{x}}\left.\frac{\partial T}{\partial \hat{x}}\right|_\eta + \right. \\
& \left. + \frac{\eta_c T' - 2T}{2\hat{x}}\left.\frac{\partial F}{\partial \hat{x}}\right|_\eta + \frac{TF'}{2\hat{x}}\left.\frac{\partial \eta_c}{\partial \hat{x}}\right|_\eta + \frac{\eta_c T}{\hat{x}}\left.\frac{\partial F'}{\partial \hat{x}}\right|_\eta + \frac{2GF'}{(2\hat{x})^{1/2}} \right) \bar{u} + \frac{\mu' T'}{3\hat{x}}\left.\frac{\partial \bar{u}}{\partial \hat{x}}\right|_\eta + \\
& + \left[\frac{(\eta_c \mu)'}{12\hat{x}^2} - \frac{\mu'}{2\hat{x}}\left.\frac{\partial T}{\partial \hat{x}}\right|_\eta \right] \frac{\partial \bar{u}}{\partial \eta} - \frac{\mu}{6\hat{x}}\frac{\partial}{\partial \hat{x}}\left(\frac{\partial \bar{u}}{\partial \eta}\right)_\eta + \frac{\eta_c \mu}{12\hat{x}^2}\frac{\partial^2 \bar{u}}{\partial \eta^2} + \left(k_z^2 \mu T - \mathrm{i}\mathcal{F} + \frac{F'}{2\hat{x}} - \frac{FT'}{2\hat{x}T} + \right. \\
& \left. - \frac{T'}{T}\left.\frac{\partial F}{\partial \hat{x}}\right|_\eta - \left.\frac{\partial F'}{\partial \hat{x}}\right|_\eta + \frac{F'}{T}\left.\frac{\partial T}{\partial \hat{x}}\right|_\eta + \frac{\eta_c F''}{2\hat{x}} \right) \bar{v} + F' \left.\frac{\partial \bar{v}}{\partial \hat{x}}\right|_\eta - \left(\frac{F}{2\hat{x}} + \left.\frac{\partial F}{\partial \hat{x}}\right|_\eta \right) \frac{\partial \bar{v}}{\partial \eta} + \\
& - \left(\frac{2\mu}{3\hat{x}T}\frac{\partial \bar{v}}{\partial \eta} \right)' + \frac{\mu' T'}{3\hat{x}}\bar{w} - \frac{\mu}{6\hat{x}}\frac{\partial \bar{w}}{\partial \eta} + \left\{ \frac{\eta_c (FF')'}{4\hat{x}^2} - \frac{FF'}{4\hat{x}^2} - \frac{F^2 T'}{4\hat{x}^2 T} - \frac{G}{(2\hat{x})^{1/2}}\frac{(F')^2}{T} + \right. \\
& \left. + \left(\frac{\mu' T' F}{3\hat{x}^2 T} \right)' - \frac{(\eta_c \mu' F'')'}{4\hat{x}^2} + \left[\frac{F'T - FT'}{2\hat{x}T} + \frac{\eta_c F''}{2\hat{x}} + \left(\frac{2\mu' T'}{3\hat{x}T} \right)' \right] \left.\frac{\partial F}{\partial \hat{x}}\right|_\eta + \left(\frac{2\mu' T'}{3\hat{x}T} + \right. \right. \\
& \left. \left. + \frac{\mu'' T'}{\hat{x}} - \frac{F}{2\hat{x}} - \frac{\eta_c F'}{2\hat{x}} \right) \left.\frac{\partial F'}{\partial \hat{x}}\right|_\eta + \frac{\mu'}{2\hat{x}}\left.\frac{\partial F''}{\partial \hat{x}}\right|_\eta + \left[\frac{FF'}{\hat{x}T} - \frac{\eta_c (F')^2}{2\hat{x}T} - \left(\frac{2\mu' F'}{3\hat{x}T} \right)' + \right.
\end{aligned}$$

$$-\frac{\mu''F''}{2\hat{x}}\Big]\left.\frac{\partial T}{\partial\hat{x}}\right|_\eta+\frac{2F'}{T}\left.\frac{\partial F}{\partial\hat{x}}\right|_\eta\left.\frac{\partial T}{\partial\hat{x}}\right|_\eta+F'\left.\frac{\partial^2F}{\partial\hat{x}^2}\right|_\eta-\frac{(F')^2}{2\hat{x}}\left.\frac{\partial\eta_c}{\partial\hat{x}}\right|_\eta-\frac{T'}{T}\left(\left.\frac{\partial F}{\partial\hat{x}}\right|_\eta\right)^2+$$
$$-\left.\frac{\partial F}{\partial\hat{x}}\right|_\eta\left.\frac{\partial F'}{\partial\hat{x}}\right|_\eta-\left.\frac{2\mu'F'}{3\hat{x}T}\frac{\partial T'}{\partial\hat{x}}\right|_\eta\Big\}\bar{\tau}-\left.\frac{\mu'F''}{2\hat{x}}\frac{\partial\bar{\tau}}{\partial\hat{x}}\right|_\eta+\left(\frac{\mu'T'F}{3\hat{x}^2T}-\frac{\eta_c\mu'F''}{4\hat{x}^2}+\right.$$
$$\left.+\left.\frac{2\mu'T'}{3\hat{x}}\frac{\partial F}{\partial\hat{x}}\right|_\eta+\frac{\mu'}{\hat{x}}\left.\frac{\partial F'}{\partial\hat{x}}\right|_\eta-\left.\frac{2\mu'F'}{3\hat{x}T}\frac{\partial T}{\partial\hat{x}}\right|_\eta\right)\frac{\partial\bar{\tau}}{\partial\eta}+\frac{1}{2\hat{x}}\frac{\partial\bar{p}}{\partial\eta}=0,\quad(2.15c)$$

$$\mathcal{Z}|\left(k_z^2T\mu'\left.\frac{\partial T}{\partial\hat{x}}\right|_\eta-k_z^2\frac{\eta_c\mu'TT'}{2\hat{x}}\right)\bar{u}+\left.\frac{k_z^2\mu T}{3}\frac{\partial\bar{u}}{\partial\hat{x}}\right|_\eta-k_z^2\frac{\eta_c\mu T}{6\hat{x}}\frac{\partial\bar{u}}{\partial\eta}+k_z^2\mu'T'\bar{v}+$$
$$+\frac{k_z^2\mu}{3}\frac{\partial\bar{v}}{\partial\eta}-\left(\mathrm{i}\mathcal{F}-\frac{4}{3}k_z^2\mu T\right)\bar{w}+\left.F'\frac{\partial\bar{w}}{\partial\hat{x}}\right|_\eta-\left(\frac{F}{2\hat{x}}+\left.\frac{\partial F}{\partial\hat{x}}\right|_\eta\right)\frac{\partial\bar{w}}{\partial\eta}-\left(\frac{\mu}{2\hat{x}T}\frac{\partial\bar{w}}{\partial\eta}\right)'+$$
$$+\left(\frac{k_z^2\mu'T'F}{3\hat{x}}+\left.\frac{2k_z^2\mu'T'}{3}\frac{\partial F}{\partial\hat{x}}\right|_\eta-\left.\frac{2k_z^2\mu'F'}{3}\frac{\partial T}{\partial\hat{x}}\right|_\eta\right)\bar{\tau}-k_z^2T\bar{p}=0,\quad(2.15d)$$

$$\mathcal{E}|\left(\left.\frac{\partial T}{\partial\hat{x}}\right|_\eta-\frac{\eta_cT'}{2\hat{x}}\right)\bar{u}-(\gamma-1)\,Ma^2\frac{\mu F''}{\hat{x}T}\frac{\partial\bar{u}}{\partial\eta}+\frac{T'}{T}\bar{v}+\left[\frac{FT'}{2\hat{x}T}-\mathrm{i}\mathcal{F}-\frac{F'}{T}\left.\frac{\partial T}{\partial\hat{x}}\right|_\eta+\right.$$
$$\left.+\frac{T'}{T}\left.\frac{\partial F}{\partial\hat{x}}\right|_\eta-(\gamma-1)\,Ma^2\frac{\mu'\,(F'')^2}{2\hat{x}T}+\frac{k_z^2\mu T}{Pr}\right]\bar{\tau}-\frac{1}{Pr}\left(\frac{\mu'T'}{2\hat{x}T}\bar{\tau}\right)'+F'\left.\frac{\partial\bar{\tau}}{\partial\hat{x}}\right|_\eta+$$
$$-\left(\frac{F}{2\hat{x}}+\left.\frac{\partial F}{\partial\hat{x}}\right|_\eta\right)\frac{\partial\bar{\tau}}{\partial\eta}-\frac{1}{Pr}\left(\frac{\mu}{2\hat{x}T}\frac{\partial\bar{\tau}}{\partial\eta}\right)'=0,\quad(2.15e)$$

where

$$G=\frac{Re^2}{r_c}=\left(\frac{\rho_\infty^*U_\infty^*}{\mu_\infty^*}\right)^2\frac{\lambda_z^{*3}}{8\pi^3r_c^*}=O(1)\qquad(2.16)$$

is the global Görtler number (Kobayashi 1972; Wu *et al.* 2011) and $\mu'\equiv\mathrm{d}\mu/\mathrm{d}T$. The global Görtler number (2.16) is defined using λ_z^* as the reference length, whereas the local Görtler number $G_\delta=(\rho_\infty^*U_\infty^*\delta_0^*/\mu_\infty^*)(\delta_0^*/r_c^*)^{1/2}$ (e.g. Floryan & Saric 1979; El-Hady & Verma 1984) is based on the boundary-layer thickness δ^* at a specified location x_0^*. The two are related by $G=G_\delta^2(\Lambda^*/\delta_0^*)^3$. The global Görtler number arises from the asymptotic scaling (2.14) and the use of λ_z^* as reference length. It distills the effect of constant disturbance spanwise wavelength and wall curvature and is independent of the growth of the laminar base flow with and without suction (Kobayashi 1972; Wu *et al.* 2011). Equations (2.15*a*)–(2.15*e*) are parabolic in $\hat{x}$ and represent an initial-boundary value problem that needs to be solved subject to appropriate initial and boundary conditions.

2.2.1. *Wall boundary conditions*

The no-slip and no-penetration conditions $\bar{u}=\bar{v}=\bar{w}=0$ are assumed over an adiabatic wall, $\partial\bar{\tau}/\partial\eta=0$ (El-Hady & Verma 1984; Viaro & Ricco 2019*a*). The use of the no-penetration condition $\bar{v}=0$ at the wall is justified as follows. In a laboratory, distributed suction is usually applied through a porous substrate where $\bar{v}$ and $\bar{p}$ are coupled via a Darcy law (e.g. Wedin

et al. 2015)

$$v^* = -\frac{K^*}{\mu^*}\frac{\partial p^*}{\partial y^*}, \tag{2.17}$$

where K^* [m^2] is the permeability. In non-dimensional form, relation (2.17) at the wall becomes

$$\hat{v}|_{y=0} = -\frac{Da\,Re}{\mu_w}\frac{\partial \hat{p}}{\partial y}\Big|_{y=0}, \tag{2.18}$$

where $\mu_w = \mu(T_w) = O(1)$ is the dynamic viscosity at the wall, the Darcy number $Da \equiv K^*/\Lambda^{*2} \ll 1$ is typically $O(Re^{-1})$ or smaller and $Da\,Re = O(1)$. Introducing the asymptotic scaling (2.14) in (2.18) leads to $\bar{v}(\partial\bar{p}/\partial\eta)^{-1} = O(Da)$, i.e. the coupling is inhibited, thus justifying the no-penetration condition at the wall.

Suction non-uniformities of small amplitude, such as those examined via linear stability analysis by Floryan (1997), Roberts *et al.* (2001) and Roberts & Floryan (2002, 2008) may alter the stability of TS waves and generate unstable streamwise vortices. The latter are not attenuated by increasing the mean suction rate. For incompressible boundary-layer flows, suction non-uniformities proportional to $\cos(\tilde{\alpha}x)$ with streamwise wavenumbers $\tilde{\alpha}$ in the unstable band $0.2 < \tilde{\alpha} < 3$ were considered. These instabilities would not occur in boundary layers over suction porous sets relevant to the present work because the pore size and spacing are $d_p^* \ll \lambda_z^*$. The corresponding suction wavenumber, $\tilde{\alpha} = 2\pi\Lambda^*/d_p^* \gg 1$, would therefore lie well outside the unstable range. The destabilizing effect of non-uniformity at the pore scale was not observed in the wind tunnel experiments of Fransson & Alfredsson (2003), Yoshioka *et al.* (2004) and Kurian & Fransson (2011).

Wall roughness can also be neglected because the roughness height is assumed to be comparable with the pore size d_p^* and, therefore, to be much smaller than the boundary-layer thickness δ^*. The use of the no-slip conditions, $\bar{u} = \bar{w} = 0$, is thus justified.

Periodic spanwise modulations of wall velocity or temperature produce finite commensurate or infinite incommensurate states, depending on the ratio of the disturbance wavenumber k_z to that of the wall modulation (Panday & Floryan 2023). Irrational ratios yield infinitely many aperiodic states, which cannot be investigated through direct numerical simulations, linear stability analysis or the present asymptotic approach due to the requirement of an infinitely wide computational domain. We therefore focus on the linear growth of a single monochromatic disturbance with constant λ_z^*, assuming a uniform suction velocity for the base flow and zero disturbance velocity at the wall.

These assumptions are consistent with the experiments of Fransson & Alfredsson (2003) who used a sintered-plastic porous layer with a permeability of $K^* = 3.7\,\mu\text{m}^2$, an average pore size of $d_p^* = 16\,\mu\text{m}$ and a roughness height of $0.38\,\mu\text{m}$. Such a low roughness is typical of polished, non-permeable surfaces used in supersonic quiet tunnels (Schneider 2008*a*).

2.2.2. *Outer boundary conditions*

Both $\bar{u}$ and $\bar{\tau}$ vanish in the free stream ($\eta \gg 1$), while $\bar{v}$, $\bar{w}$ and $\bar{p}$ satisfy boundary conditions of the mixed type

$$\frac{\partial\bar{v}}{\partial\eta} + |k_z|\,(2\hat{x})^{1/2}\,\bar{v} \to -\mathrm{e}^{\mathrm{i}\mathcal{F}\hat{x}+\mathrm{i}k_y(2\hat{x})^{1/2}[\eta-\beta_c(\hat{x})]-\left(k_y^2+k_z^2\right)\hat{x}}, \tag{2.19a}$$

$$\frac{\partial\bar{w}}{\partial\eta} + |k_z|\,(2\hat{x})^{1/2}\,\bar{w} \to \mathrm{i}k_y\,(2\hat{x})^{1/2}\,\mathrm{e}^{\mathrm{i}\mathcal{F}\hat{x}+\mathrm{i}k_y(2\hat{x})^{1/2}[\eta-\beta_c(\hat{x})]-\left(k_y^2+k_z^2\right)\hat{x}}, \tag{2.19b}$$

$$\frac{\partial\bar{p}}{\partial\eta} + |k_z|\,(2\hat{x})^{1/2}\,\bar{p} \to 0, \tag{2.19c}$$

which differ from the those used by LWG99, Ricco & Wu (2007) and Viaro & Ricco (2019*a*) because the term $\beta_c(\hat{x}) = \lim_{\eta\to\infty}[\eta - F(\hat{x},\eta)]$ is streamwise-dependent.

The outer boundary conditions (2.19) are derived by matching the outer limit of region III (i.e. the large-η limit of the CLUBR equations (2.15*a*)–(2.15*e*)) with the inner limit of region IV. Following Wundrow & Goldstein (2001), the flow in region IV - where $\hat{x}, \hat{y} = O(1)$ and $\hat{y} = Re^{-1}y$ - is decomposed in its steady two-dimensional and unsteady three-dimensional parts at $O(\epsilon)$

$$\boldsymbol{u} = \{1,0,0\} + \epsilon\{\acute{u},\acute{v},0\}(\hat{x},\hat{y}) + \epsilon\{\grave{u},\grave{v},\grave{w}\}(\hat{x},y,\hat{y},z,\hat{t}) + \dots \tag{2.20a}$$

$$p = \frac{1}{\gamma Ma^2} + \epsilon\acute{p}(\hat{x},\hat{y}) + \epsilon^2\grave{p}(\hat{x},y,\hat{y},z,\hat{t}) + \dots \tag{2.20b}$$

$$\tau = 1 + \epsilon\acute{\tau}(\hat{x},\hat{y}) + \epsilon\grave{\tau}(\hat{x},y,\hat{y},z,\hat{t}) + \dots \tag{2.20c}$$

By introducing the expansion (2.20) in the Navier-Stokes and perfect gas equations, one finds a system of equations for the steady, two-dimensional and the unsteady, three-dimensional part of the flow in region IV. The steady two-dimensional part $\{1,0,0\} + \epsilon\{\acute{u},\acute{v},0\}(\hat{x},\hat{y})$ is induced by the base-flow displacement and is governed by the steady Euler equations. Its wall-normal velocity component $\epsilon\acute{v}$ matches the base flow velocity V (2.11*b*) when $r_t \ll 1$

$$\lim_{\hat{y}\to 0}\epsilon\acute{v} = \lim_{\eta\to\infty} V = \frac{1}{Re}\frac{\mathrm{d}}{\mathrm{d}\hat{x}}\left[(2\hat{x})^{1/2}\beta_c(\hat{x})\right] + \frac{1}{Re}\frac{\gamma_c(\hat{x})}{(2\hat{x})^{1/2}}, \tag{2.21}$$

where $\gamma_c(\hat{x}) = \lim_{\eta\to\infty}(\eta_c - \eta)$. The streamfunction for the first two terms in (2.20*a*) is $\Psi(\hat{x},y,\hat{y}) = y + \psi_1(\hat{x},\hat{y})$, where

$$\epsilon\acute{v} = -\frac{1}{Re}\frac{\partial\psi_1}{\partial\hat{x}} = -\frac{1}{Re}\frac{\partial\Psi}{\partial\hat{x}}. \tag{2.22}$$

Equating (2.21) and (2.22) and integrating yields

$$\Psi(\hat{x},y) = y - (2\hat{x})^{1/2}\beta_c(\hat{x}) - \int^{\hat{x}}\frac{\gamma_c(\check{x})}{(2\check{x})^{1/2}}\mathrm{d}\check{x}, \text{ for } \hat{y}\ll 1,\ y = O(1). \tag{2.23}$$

The streamfunction ψ_1 valid for all $\hat{x}$ and $\hat{y}$ is obtained by solving a Laplace equation (in the subsonic case) or a wave equation (in the supersonic case). More details on the derivation of the equation for ψ_1 are in appendix A. Note that an analytical expression for $\psi_1(\hat{x},\hat{y})$ cannot be obtained for all $\hat{y}$ in the non-similar case nor when the self-similar base flow is supersonic. However, the outer boundary conditions (2.19) are derived by matching the large-η limit of the CLUBR equations (2.15*a*)–(2.15*e*) with the small-$\hat{y}$ limit of $\{\grave{u},\grave{v},\grave{w}\}$ in (2.20*a*) (LWG99). Hence, the focus is on the asymptotic behaviour of ψ_1 as $\hat{y}\to 0$ (i.e. $\hat{y}\ll 1$) given in (2.23).

The unsteady, three-dimensional part of (2.20) is governed by

$$C|\ \frac{\partial\grave{v}}{\partial y} + \frac{\partial\grave{w}}{\partial z} = 0, \tag{2.24a}$$

$$\mathcal{Y}|\ \frac{\partial\grave{v}}{\partial\hat{t}} + \frac{\partial\grave{v}}{\partial\hat{x}} + r_t\left[(\acute{v}+\grave{v})\frac{\partial\grave{v}}{\partial y} + \grave{w}\frac{\partial\grave{v}}{\partial z} + \frac{\partial\grave{p}}{\partial y}\right] = \frac{\partial^2\grave{v}}{\partial y^2} + \frac{\partial^2\grave{v}}{\partial z^2}, \tag{2.24b}$$

$$\mathcal{Z}|\ \frac{\partial\grave{w}}{\partial\hat{t}} + \frac{\partial\grave{w}}{\partial\hat{x}} + r_t\left[(\acute{v}+\grave{v})\frac{\partial\grave{w}}{\partial y} + \grave{w}\frac{\partial\grave{w}}{\partial z} + \frac{\partial\grave{p}}{\partial z}\right] = \frac{\partial^2\grave{w}}{\partial y^2} + \frac{\partial^2\grave{w}}{\partial z^2}, \tag{2.24c}$$

$\grave{u} = \grave{\tau} = 0$, and $\grave{\rho} = 0$ because of the perfect gas equation. The system (2.24) is elliptic in the cross-flow (y-z) plane and the viscous three-dimensional components are coupled to

the inviscid two-dimensional ones because $\acute{v}$ appears in (2.24). The velocity components are decoupled by substituting (2.22) and (2.23) into (2.24), which yields the linearised momentum balances valid for $\hat{y} \ll 1$ (LWG99),

$$\left(\frac{\partial}{\partial \hat{t}} + \frac{\partial}{\partial \hat{x}}\bigg|_{\Psi} - \frac{\partial^2}{\partial \Psi^2} - \frac{\partial^2}{\partial z^2}\right)\{\hat{v}, \hat{w}\} = 0. \tag{2.25}$$

The solution to (2.25) is

$$\{\hat{v}, \hat{w}\}\left(\hat{x}, \Psi, z, \hat{t}\right) = \{\hat{v}, \hat{w}\}\left(\hat{x}\right) \mathrm{e}^{-\mathrm{i}\mathcal{F}\hat{t}+\mathrm{i}k_y\Psi+\mathrm{i}k_z z} + \mathrm{c.c.}, \tag{2.26}$$

where the amplitude is found by matching with (2.1) for $\Psi \sim y = O(1)$ and $\hat{x} \ll 1$,

$$\{\hat{v}, \hat{w}\}\left(\hat{x}\right) = \{\hat{v}^{\infty}, \hat{w}^{\infty}\}\, \mathrm{e}^{\mathrm{i}\mathcal{F}\hat{x}-\left(k_y^2+k_z^2\right)\hat{x}}. \tag{2.27}$$

As $T \sim 1$ and $\bar{Y} = O(y)$ for $y, \eta \gg 1$, the far-field variable for region III, $y^{(0)}$, is defined consistently with (2.23)

$$y^{(0)} \equiv \left(2\hat{x}\mathcal{F}\right)^{1/2}\left[\eta - \beta_c\left(\hat{x}\right)\right] - \mathcal{F}^{1/2}\int^{\hat{x}} \frac{\gamma_c\left(\check{x}\right)}{\left(2\check{x}\right)^{1/2}}\mathrm{d}\check{x}. \tag{2.28}$$

By applying the transformation $(\hat{x}, \eta) \rightarrow (\hat{x}, y^{(0)})$ to the large-η form of (2.15*a*)–(2.15*e*), the far-field equations are recovered,

$$C|\left(2\hat{x}\mathcal{F}\right)^{1/2}\frac{\partial \bar{v}}{\partial y^{(0)}} + \bar{w} = 0, \tag{2.29a}$$

$$\mathcal{Y}|\left(\frac{1}{2\hat{x}} + k_z^2 - \mathrm{i}\mathcal{F}\right)\bar{v} + \frac{\partial \bar{v}}{\partial \hat{x}}\bigg|_{y^{0)}} - \frac{\mathcal{F}^{1/2}\gamma_c(\hat{x})}{\left(2\hat{x}\right)^{1/2}}\frac{\partial \bar{v}}{\partial y^{(0)}} - \mathcal{F}\frac{\partial^2 \bar{v}}{\partial y^{(0)2}} + \frac{\mathcal{F}^{1/2}}{\left(2\hat{x}\right)^{1/2}}\frac{\partial \bar{p}}{\partial y^{(0)}} = 0, \tag{2.29b}$$

$$\mathcal{Z}|\left(k_z^2 - \mathrm{i}\mathcal{F}\right)\bar{w} + \frac{\partial \bar{w}}{\partial \hat{x}}\bigg|_{y^{(0)}} - \frac{\mathcal{F}^{1/2}\gamma_c(\hat{x})}{\left(2\hat{x}\right)^{1/2}}\frac{\partial \bar{w}}{\partial y^{(0)}} - \mathcal{F}\frac{\partial^2 \bar{w}}{\partial y^{(0)2}} - k_z^2\bar{p} = 0. \tag{2.29c}$$

The solution (2.19) that matches with (2.1) for $\hat{x} \ll 1$, $y^{(0)} = O(1)$ and (2.26) for $\hat{x} = O(1)$, $y^{(0)} \gg 1$ is first derived for $\bar{p}$ by combining the wall-normal derivative of (2.29*b*) with (2.29*c*) and using (2.29*a*). The spanwise component $\bar{w}$ is obtained by solving the inhomogeneous heat equation

$$\frac{\partial \bar{w}^0}{\partial \hat{x}}\bigg|_{\hat{y}^{(0)}} - \mathcal{F}\frac{\partial^2 \bar{w}^0}{\partial \hat{y}^{(0)2}} = k_z^2\bar{p}\mathrm{e}^{\left(k_z^2-\mathrm{i}\mathcal{F}\right)\hat{x}}, \tag{2.30}$$

where the change of variable $\bar{w} = \bar{w}^0\mathrm{e}^{\left(\mathrm{i}\mathcal{F}-k_z^2\right)\hat{x}}$, $\hat{y}^{(0)} = \left(2\hat{x}\mathcal{F}\right)^{1/2}\left[\eta - \beta_c\left(\hat{x}\right)\right]$ was used to simplify (2.29*c*) (Polyanin & Nazaikinskii 2015, §3.8.7.4). Equation (2.30) is solved with initial conditions derived by matching $\bar{v}$ and $\bar{w}$ to region I (2.1), while the outer conditions are established by matching $\bar{v}$ and $\bar{w}$ to the small-$\hat{y}$ limit of region IV (2.26). The wall-normal component $\bar{v}$ is derived by integrating (2.29*a*).

2.2.3. *Initial conditions*

The initial conditions are imposed in the impermeable region at $\hat{x} \ll 1$ and are therefore those of Viaro & Ricco (2019*a*, appendix B). The evolution from the impermeable to the suction region occurs gradually across an adjustment strip of finite width $\Delta\hat{x}_s$ (red area in figure 1) and centred at a prescribed $\hat{x}_s$. In this region, the suction velocity varies as $V_w S(\hat{x})$,

where

$$S(\hat{x}) = \begin{cases} 0, & \text{for } \hat{x} - \hat{x}_s \leqslant -\Delta\hat{x}_s/2, \\ \left[1 + \exp\left(\dfrac{1}{\tilde{x}-1} + \dfrac{1}{\tilde{x}}\right)\right]^{-1}, & \text{for } |\hat{x} - \hat{x}_s| \leqslant \Delta\hat{x}_s/2, \\ 1, & \text{for } \hat{x} - \hat{x}_s > \Delta\hat{x}_s/2, \end{cases} \tag{2.31}$$

and $\tilde{x} = (\hat{x} - \hat{x}_s + \Delta\hat{x}_s/2)/\Delta\hat{x}_s$ (Negi *et al.* 2015). We have verified that varying the length of the adjustment strip between $\Delta\hat{x}_s = 0.01$ and 0.1 has a negligible effect on the results. We assume $\Delta\hat{x}_s = 0.05$ for all the computations. In the results section, γ_w indicates the constant suction value attained at the end of the adjustment strip.

2.2.4. *Numerical procedures*

The base flow and the CLUBR equations are solved by marching downstream as they are parabolic in $\hat{x}$. At each $\hat{x}$ location, the solution is obtained by a second-order accurate block-elimination algorithm (Cebeci 2002), also used to solve (2.13). When suction is applied, the boundary layer becomes thinner in η and thus a non-uniform grid is used to resolve the near-wall region. More details on the numerical method are found in appendix B.

3. Results

The base-flow solution (2.5) is validated in §3.1.1 against wind-tunnel measurements and direct numerical simulations of boundary layers with uniform suction. The free-stream conditions outlined in table 1 are used in the rest of §3. The characteristics of the porous wall and the base-flow properties are discussed in §3.1.2 and §3.1.3, respectively. The combined effect of receptivity and uniform suction on the growth of Görtler vortices is studied in §3.2. The neutral curves are examined in §3.3.

3.1. *Laminar base flow*

3.1.1. *Comparison with experiments and direct numerical simulations*

The non-similar laminar base flow (2.5) with wall suction is validated against the low-speed wind tunnel data of Fransson & Alfredsson (2003) (figure 3, a). The free-stream velocity is $U^*_\infty = 5\,\mathrm{m\,s^{-1}}$ and a region of uniform suction velocity $V^*(\hat{x}, 0) = -1.44\,\mathrm{cm\,s^{-1}}$ begins at $x^*_s = 0.36\,\mathrm{m}$. We assume a spanwise wavelength $\lambda^*_z = \delta^*_{99}(x^*_s) = 5.2\,\mathrm{mm}$, which yields $Re = 275$ and $\gamma_w = -0.79$. The results of (2.5) (figure 3, a) show excellent agreement with the wind tunnel data. At $x^* = 0.9\,\mathrm{m}$, the boundary layer reaches the asymptotic-suction state, denoted by the black bold curve of the incompressible asymptotic-suction profile $U = 1 - \exp(\gamma_w y)$. Fransson & Alfredsson (2003) had previously validated their results by solving a non-similar incompressible boundary-layer equation with a sharp transition from the impermeable to the suction region, i.e. without the smooth adjustment strip described in §2.2.3 ($\Delta\hat{x}_s = 0$). Their mathematical formulation differs in that it features the streamwise variable $\xi = \gamma_w \hat{x}^{1/2}$ and the scalings $F(\xi, \eta) = \psi(\hat{x}, y)\gamma_w \xi^{-1}$ and $\eta = y\gamma_w \xi^{-1}$, all dependent on the suction rate γ_w.

A good agreement is also found with the wind-tunnel data of Kay (1953) (figure 3, b). They studied an incompressible boundary layer with $U^*_\infty = 17.37\,\mathrm{m\,s^{-1}}$ and developing over a porous surface. The boundary-layer thickness was $\delta^*_{99} = 1.5\mathrm{mm}$ at the beginning of the suction region, located at $x^*_s = 0.11\mathrm{m}$, the kinematic viscosity was $\nu^* = 1.43 \cdot 10^{-5}\,\mathrm{m^2/s}$ and the Reynolds number based on δ^*_{99} was 290. A uniform suction velocity $V(\hat{x}, 0) = -5.1\,\mathrm{cm\,s^{-1}}$ was applied and the laminar asymptotic suction profile was attained at $x^* = 0.35\,\mathrm{m}$.

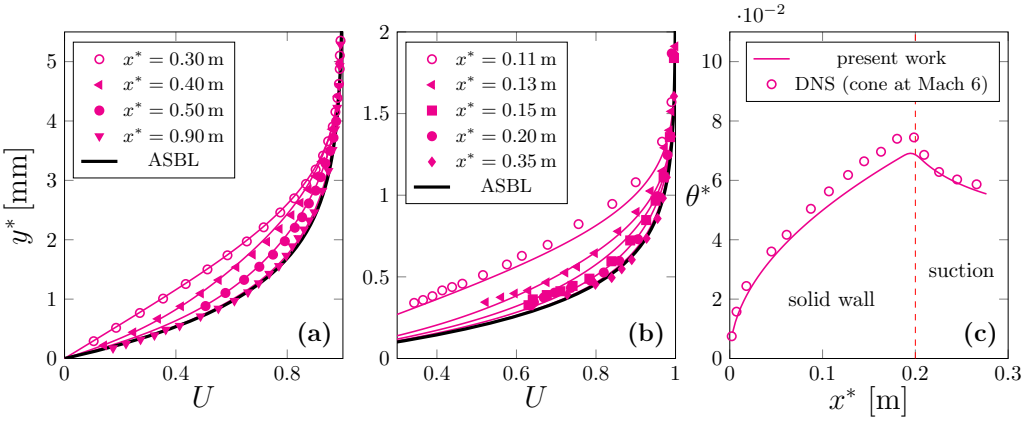

Figure 3: Left (a) and centre (b): laminar velocity profiles in the suction region (solid curves) compared with the incompressible data (marks) of Fransson & Alfredsson (2003) (a, $x_s^* = 0.34\,\mathrm{m}$) and Kay (1953) (b, $x_s^* = 0.11\,\mathrm{m}$). Asymptotic-suction profiles are plotted in bold black. Right (c): momentum thickness along the surface of a cone at Mach 6 and the numerical data of Hollender *et al.* (2019) ($x_s^* = 0.2\,\mathrm{m}$).

The velocity and temperature profiles of compressible laminar boundary layers over porous plates with suction are not readily available in the experimental and numerical literature. The wall-normal profiles reported in Leontiev & Pavlyuchenko (2008) at $Ma = 2.5$ cannot be used for comparison because they were measured in a high-intermittency region downstream of a perforated suction plate, where the flow was already transitional. Hollender *et al.* (2019) performed direct numerical simulations on the cone-flared cone geometry studied by Li *et al.* (2018). Unfortunately, we are unable to validate our computations against the velocity profile they sampled in the suction region as neither the corresponding boundary-layer thickness nor the exact location of the suction region on the cone was specified. Nevertheless, Hollender *et al.* (2019) reported the distribution of the momentum thickness upstream of and over the suction region. They imposed a constant mass flow rate $\dot{m}_{sur}^* = -0.5\,\mathrm{g\,s^{-1}}$ on the surface of a truncated section of a cone with a half-angle $\alpha_{cone} = 7°$. The fore section of the model was conical and had a slant height of 0.3 m. The suction region was located between $\ell_1^* = 0.20\,\mathrm{m}$ and $\ell_2^* = 0.28\,\mathrm{m}$ from the tip and covered an estimated area

$$A_{suc}^* = \pi\left(\ell_1^* + \ell_2^*\right)\sin\left(\alpha_{cone}\right)\left(\ell_2^* - \ell_1^*\right) = 0.0147\,\mathrm{m}^2. \tag{3.1}$$

The free-stream density and temperature were $\rho_\infty^* = 0.035\,\mathrm{kg/m^3}$ and $T_\infty^* = 52.6\,\mathrm{K}$. The boundary layer on the cone at zero angle of attack develops downstream of an axisymmetric conical shock wave, with no fluid motion occurring along the meridian planes. The inviscid flow properties at the cone surface are described by the Taylor-Maccoll theory and the boundary layer is governed by the compressible Blasius solution (Stewartson 1964). For $Ma = 6$ and $\alpha_{cone} = 7.5°$, the tables in Sims (1964) report the following thermodynamic properties at the cone surface

$$\frac{p_{sur}^*}{p_\infty^*} = 2.08, \quad \frac{\rho_{sur}^*}{\rho_\infty^*} = 1.68, \quad \frac{T_{sur}^*}{T_\infty^*} = 1.24, \quad Ma_{sur} = 5.3.$$

The inviscid surface velocity is $U_{sur}^* = Ma_{sur}\sqrt{\gamma\mathcal{R}^* T_\infty^*} = 857.53\,\mathrm{m\,s^{-1}}$. Assuming $\lambda_z^* = \delta_{99}^* = 1\,\mathrm{mm}$ (Li *et al.* 2018), the Reynolds number is $Re_{sur} = \rho_{sur}^* U_{sur}^* \lambda_z^* / (2\pi\mu_{sur}^*)$, where

Table 1: Free-stream conditions reported in wind-tunnel tests over impermeable surfaces. Cited studies are Flechner *et al.* (1976, F76), Graziosi & Brown (2002, GB02), Maslov *et al.* (2001, M01), Running *et al.* (2023, R23), Tani (1962, T62), Finnis & Brown (1997, FB97), Ciolkosz & Spina (2006, CS06), Wang *et al.* (2018, W18), Li *et al.* (2018, L18) and de Luca *et al.* (1993, L93). The flow conditions used in §3.2 and §3.3 are highlighted in pink. The subscript o denotes the stagnation quantities.

Ref.	type	Ma	p_o^* [kPa]	T_o^* [K]	p_∞^* [kPa]	T_∞^* [K]	Re_u^* [10^6m^{-1}]
F76	flat plate	0.8	97	322	64	284	10.7
GB02	flat plate	2.98	32	290	0.9	104	2.62
M01	flat plate	5.92	1080	390	0.74	49	19.4
R23	flat plate	6.1	490 to 3044	458 to 488	0.28 to 1.74	54.25 to 57.81	6.3 to 35.3
T62	concave plate	0.03	101325	303.15	101325	303.15	0.687
FB97	concave plate	0.02	101325	293.15	101325	293.15	0.5 to 0.6
CS06	concave plate	1.06 to 2.87	n.a.	n.a.	n.a.	n.a.	41.8 to 59.6
W18	concave plate	2.95	85.2	288	2.5	105	7.15
L18	flared cone	6	1109	426	0.71	52	12.9
L93	concave plate	7	4500 to 10^4	800	1.82 to 4.05	74	12.9 to 28.6

the viscosity at the surface is estimated using Sutherland's law

$$\frac{\mu^*}{\mu^*_{ref}} = \left(\frac{T^*}{T_{ref}}\right)^{3/2} \frac{\chi^* + T^*_{ref}}{\chi^* + T^*}, \tag{3.2}$$

with $\mu^*_{ref} = 1.85 \cdot 10^{-5}$ Pa s, $T^*_{ref} = 300$ K, $\chi^* = 129$ K. The adiabatic recovery temperature is (Anderson 2016)

$$T^*_w = T^*_{sur}\left(1 + \frac{\gamma - 1}{2} Pr^{1/2} Ma^2_{sur}\right) = 374\,\text{K}. \tag{3.3}$$

The wall-normal velocity is found from the mass flow rate $\dot{m}^*_w$

$$V^*_w = \frac{\dot{m}^*_w}{\rho^*_w A^*_{suc}} = \frac{\dot{m}^*_w}{A^*_{suc}} \frac{T^*_w}{\rho^*_{sur} T^*_{sur}}. \tag{3.4}$$

The surface temperature of the cone is $T^*_w = 300$ K and the suction parameter is

$$\gamma_w = \frac{\dot{m}^*_w}{A^*_{suc}} \frac{T^*_w}{T^*_{sur}} \frac{\lambda^*_z}{2\pi\mu^*_{sur}} = -6.01. \tag{3.5}$$

The boundary-layer momentum thickness is computed from our base-flow solution (2.5)

$$\theta_{BL} = \int_0^\infty \frac{U}{T}\,(1 - U)\,\mathrm{d}y, \tag{3.6}$$

and agrees well with the DNS results, as shown in figure 3 (c).

3.1.2. *Suction rates through the porous wall*

The results presented from this point onwards are computed using the free-stream conditions of cases F76 and W18 in table 1. Since suction is typically achieved by generating a pressure gradient across a porous membrane, the implementation of a transpiration surface is constrained by the low static pressures in supersonic wind tunnels. Therefore, one might question whether the values of γ_w considered herein are feasible in practice. Although the

Table 2: Properties of the flow within the porous wall from Flechner *et al.* (1976, F76) and Wang *et al.* (2018, W18).

Ref.	Ma -	Kn -	γ_w -	Re_d (3.7) -	Δp^* [Pa]	$\partial p^*/\partial y^*$ [kPa/m]	Δh^* (3.8) [mm]
F76	0.8	0.007	−2	0.083	63634	715	89.1
			−5	0.210		182	35.6
W18	2.95	0.090	−2	0.017	2500	1437	1.7
			−5	0.043		3597	0.7
			−10	0.087		7018	0.3

design of suction actuators is beyond the scope of this work, we provide an estimate of the membrane's thickness in this section. The velocity through the porous layer is assumed to be uniform and equal to V_w and the flow is governed by the linear Darcy law (2.17) (Schmidt *et al.* 2016; Traub *et al.* 2024). The use of (2.17) is justified when the pore-scale Reynolds number is sufficiently small

$$Re_d \equiv \frac{\rho_w^* V_w^* d_p^*}{\mu_w^*} = \frac{p_\infty^*}{\mathcal{R}^* T_w^*} \frac{\gamma_w U_\infty^*}{Re} \frac{d_p^*}{\mu_w^*} \ll 1. \tag{3.7}$$

In (3.7), T_w^* is computed using (3.3) with T_∞^* and Ma instead of T_{sur}^* and Ma_{sur}. The effect of choking, which may be important at high suction rates (Li *et al.* 2018), is not considered (Schmidt *et al.* 2016). The pore diameter and permeability of Fransson & Alfredsson (2003), $d_p^* = 16\,\mu\text{m}$ and $K^* = 3.7 \cdot 10^{-12}\,\text{m}^2$, are used. The combination of low pressure and high recovery temperature yields a relatively high mean-free path $\ell_{mfp}^* = (\pi \mathcal{R}^* T_w^*/2)^{1/2} \mu_w^*/p_\infty^*$ and Knudsen number based on the pore diameter $Kn = \ell_{mfp}^*/d_p^*$. The flow within the pores lies in the slip regime ($0.001 < Kn \leqslant 0.1$) and the permeability is enhanced by a factor $1 + 7.23Kn$ (Yang & Weigand 2018). The theoretical maximum pressure difference across a porous layer of thickness Δh^* is the static pressure in the free stream, $\Delta p^* = p_\infty^*$, if one assumes that a steady vacuum is generated underneath. Assuming $\partial p^*/\partial y^* \cong \Delta p^*/\Delta h^*$, the Darcy law (2.17) becomes

$$\frac{\Delta h^*}{p_\infty^*} = -\frac{K^*\,(1 + 7.23Kn)}{\mu_w^*} \frac{Re}{\gamma_w U_\infty^*}, \tag{3.8}$$

where Δh^* represents the maximum theoretical thickness of the porous layer through which a given suction rate γ_w can be realised assuming that a vacuum is generated underneath.

The estimated maximum thicknesses pertinent to the considered range of γ_w are shown in the rightmost column in table 2 along with the pore-scale Reynolds number and the Knudsen number. In all cases, Kn is within the limits of the slip regime and Re_d is much smaller than unity. The value of Δh^* decreases dramatically in the supersonic case due to the higher γ_w, higher T_w^* and lower p_∞^*. The smallest thickness $\Delta h^* = 348\,\mu\text{m}$ corresponds to the case $Ma = 2.95$ and $\gamma_w = -10$, and is about 21 times d_p^*.

3.1.3. *Compressible boundary layers*

The streamwise evolution of the base flow profiles at $Ma = 0.80$ (F76) and $Ma = 2.95$ (W18) are shown in figures 4 and 5, respectively. As the wall is adiabatic and $\hat{x}_s$ and $\Delta\hat{x}_s$ are fixed, the behaviour of the laminar base flow is determined by γ_w and Ma. The ASBL profiles (red circles) are obtained by solving the system (2.13). The profiles of U and T shown in figure 4 and 5 are sampled at $\hat{x} = 0.1$ and $\hat{x} = 0.3$ and represent the suction (red) and no-suction

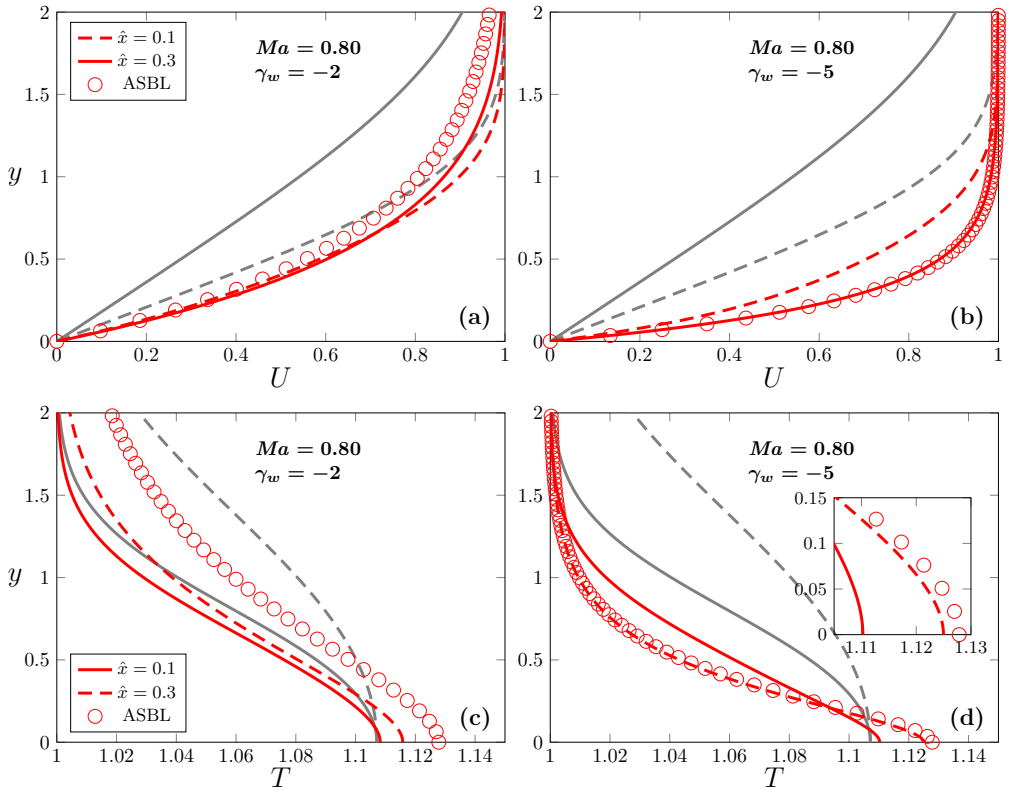

Figure 4: Effect of uniform suction on the velocity and temperature base-flow profiles at $Ma = 0.80$ and for different $\hat{x}$. The no-suction cases (self-similar base flow) are plotted in gray for comparison. The evolution of the velocity U (a, b) and temperature T (c, d) profiles is shown for $\gamma_w = -2$ (a, c) and $\gamma_w = -5$ (b, d). The asymptotic suction profiles are plotted with the circles.

(gray) cases. While the velocity and temperature profiles without suction become thicker in y when suction is absent and the solution is self-similar, they remain close to the wall and adjust to the ASBL when suction is applied.

When suction is mild, such as for $\gamma_w = -2$ at $Ma = 0.80$ (figure 4, left) or $\gamma_w = -5$ at $Ma = 2.95$ (figure 5, right), the boundary-layer thickens over the suction region before reaching the ASBL state. Moreover, for these values of γ_w and Ma, the temperature adjusts to the ASBL conditions more gradually than the velocity. The opposite occurs for intense suction, such as for $\gamma_w = -5$ at $Ma = 0.80$ (figure 4, left) or $\gamma_w = -10$ at $Ma = 2.95$ (figure 5, right), in which cases the boundary-layer thickness decreases downstream of $\hat{x}_s$. A thinning boundary layer is also observed in the direct numerical simulations of Hollender *et al.* (2019) (figure 3, right). The streamwise distance along which the Blasius profile shifts to the asymptotic-suction profile becomes shorter as γ_w increases and Ma is fixed. Even when γ_w is intense, the streamwise-evolving temperature profile and the ASBL temperature profile still differ slightly near the wall, even though the streamwise velocity profiles show excellent collapse (insets in figures 4d and 5d).

For a given γ_w, the effect of suction weakens as the Mach number and the wall temperature increase. For instance, the same suction rate $\gamma_w = -5$ produces a slower adjustment at $Ma = 2.95$ than at $Ma = 0.80$ from the Blasius boundary layer to the ASBL. A higher

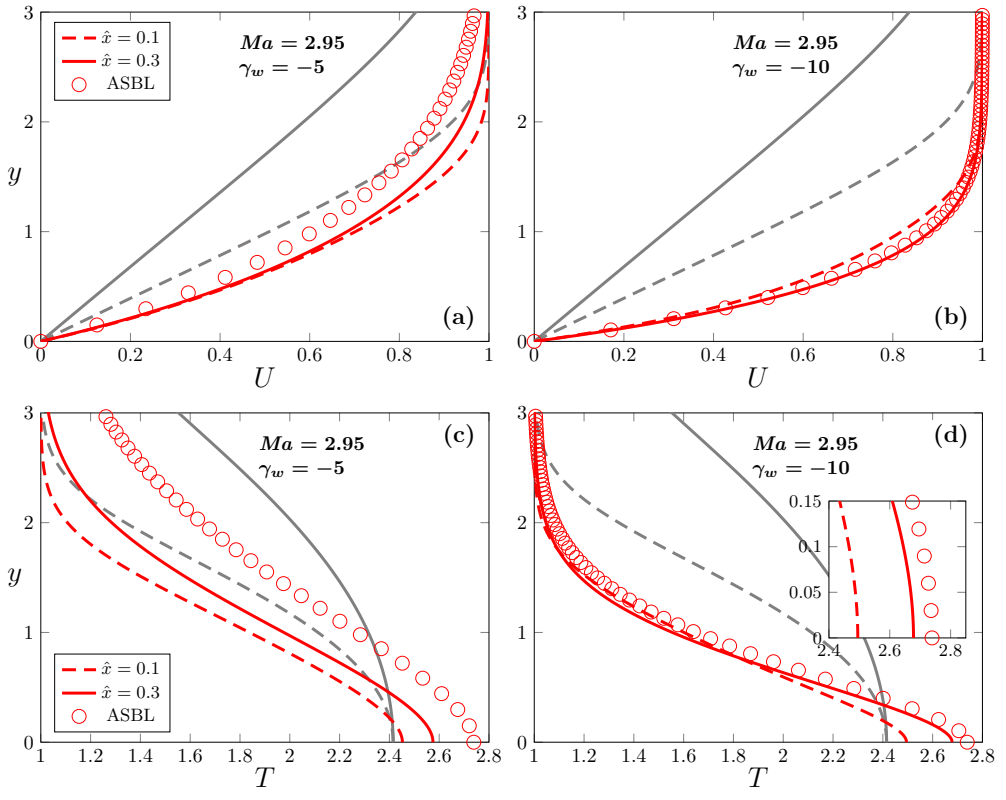

Figure 5: Effect of uniform suction on the velocity and temperature base-flow profiles at $Ma = 2.95$ and for different $\hat{x}$. The no-suction cases (self-similar base flow) are plotted in gray for comparison. The evolution of the velocity U (a, b) and temperature T (c, d) profiles is shown for $\gamma_w = -5$ (a, c) and $\gamma_w = -10$ (b, d). The asymptotic suction profiles are plotted with the circles.

wall temperature $T_w = T(\hat{x}, 0)$ decreases the amplitude of the forcing term in the boundary condition (2.12), and a given V_w generates a lower mass flow rate through the wall when Ma is higher.

3.2. *Attenuation of compressible Görtler vortices*

The effect of suction on the receptivity to steady free-stream vorticity is examined. In this section, the geometry is fixed. We consider a typical $r_c^* = 5$ m for the subsonic case (Viaro & Ricco 2019*a*) and take $r_c^* = 1$ m as in the experiments of W18 for the supersonic case. The free-stream conditions of F76 and W18 are adopted (with fixed $k_y = 1$) and we study the effect of different γ_w and λ_z^* on the boundary-layer perturbations. For given free-stream conditions and wall curvature, varying γ_w impacts the base flow only, while varying λ_z^* changes Re and G (the latter grows with the third power of λ_z^*, as given in (2.16)).

The evolution of the amplitudes of the streamwise velocity and temperature perturbations is shown in figure 6 for $\lambda_z^* = 1$ mm (magenta) and 2 mm (orange) as a function of x^*/x_s^*. Suction markedly attenuates the growth of the streamwise velocity and temperature fluctuations ($|\bar{u}|$ and $|\bar{\tau}|$ are multiplied by Re in figure 6 to study quantities that are proportional to the physical variables in (2.14) as λ_z^* varies). The attenuation effect of suction intensifies as γ_w increases, although it weakens as the conditions changes from subsonic to supersonic, in qualitative

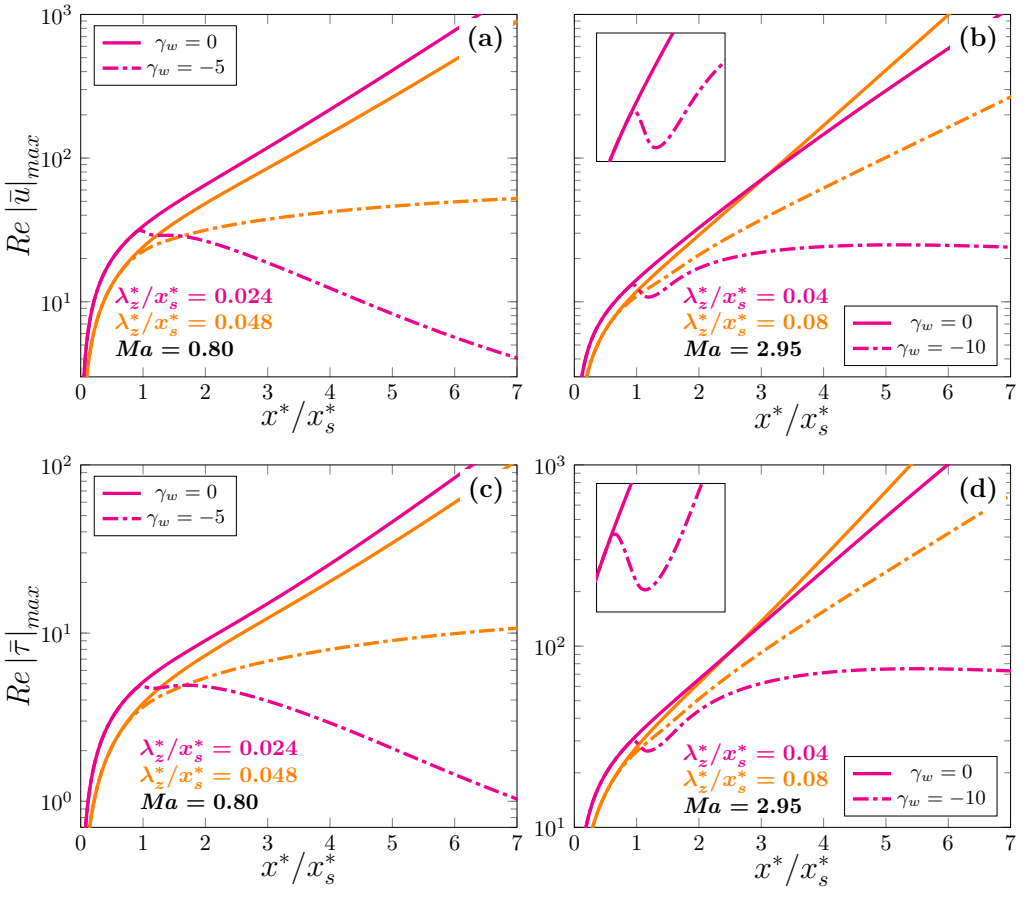

Figure 6: Uniform suction: effect of γ_w and λ_z^* on the maximum of the streamwise-velocity disturbances (a, b) and the temperature disturbances (c, d) in steady conditions at $Ma = 0.8$ (a, c) and $Ma = 2.95$ (b, d). The length of the impermeable region is $x_s^* = 4.2$ cm in the subsonic case and $x_s^* = 2.5$ cm in the supersonic case. The magenta and orange curves show the cases $\lambda_z^* = 1$ mm and 2 mm, respectively.

agreement with the results of linear stability theory (El-Hady & Verma 1984). In the high-subsonic case (figure 6, left), a suction rate of $\gamma_w = -5$ turns exponentially-growing Görtler vortices with $\lambda_z^* = 1$ mm into decaying laminar streaks. In the supersonic case, an intense suction rate of $\gamma_w = -10$ renders the perturbations constant along the streamwise direction. A transient behaviour is observed around x_s^* in the supersonic case for $\gamma_w = -10$ (refer to inset in the top right plot of figure 6). The disturbance amplitude rapidly decreases, reaches a minimum downstream and then increases again under the forcing exerted by free-stream vorticity.

In the absence of suction, increasing λ_z^* delays the onset of Görtler vortices. The delay occurs because the condition for large centrifugal growth is weakened, i.e. δ^* becomes comparable with λ_z^* further downstream and thus the role of the $\mathcal{Y}$-momentum balance, where the centrifugal effect is active, is postponed. The influence of suction on the growth of Görtler vortices decreases as λ_z^* increases, in both subsonic and supersonic conditions.

The normalised velocity and temperature perturbation profiles at different streamwise locations are plotted in figure 7 for $\gamma_w = 0$ (solid curves, a and b), $\gamma_w = -5$ (subsonic, a) and

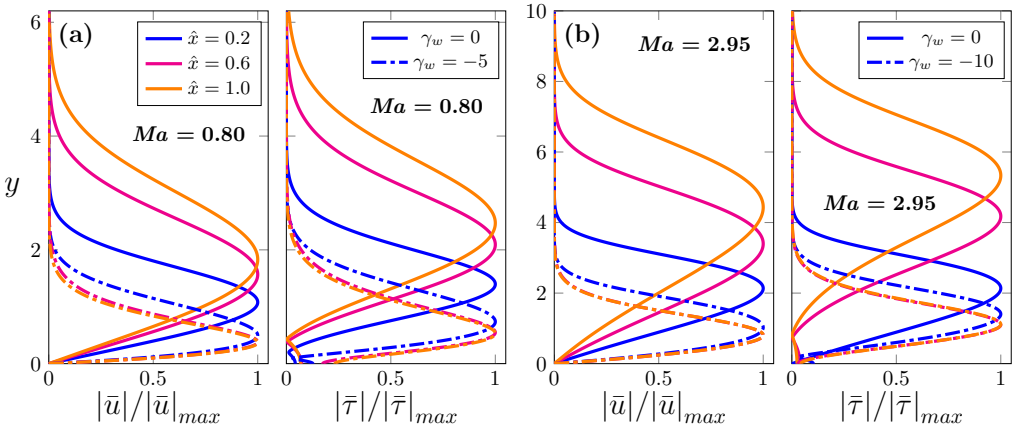

Figure 7: Perturbation velocity and temperature with (dash dot) and without (solid) suction at $Ma = 0.80$ (a) and $Ma = 2.95$ (b).

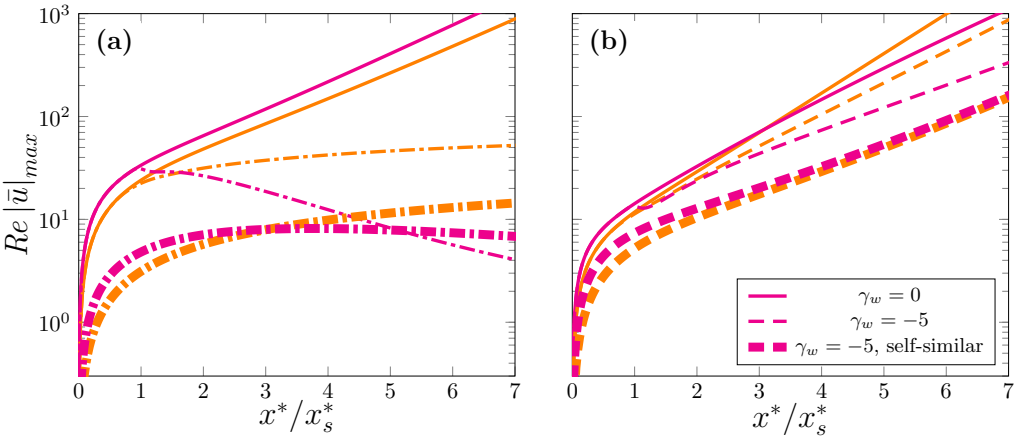

Figure 8: Comparison with self-similar suction: effect of γ_w and λ_z^* on the maximum of the streamwise-velocity disturbances in steady conditions at $Ma = 0.8$ (a) and $Ma = 2.95$ (b). The magenta and orange curves show the cases $\lambda_z^* = 1$ mm and 2 mm, respectively.

$\gamma_w = -10$ (supersonic, b). The peaks of the fluctuations move to higher y (but lower η) as the boundary layer thickens when suction is absent or mild. When suction is intense enough to induce the decay of the streaks, the shape of the normalised perturbation profiles is unaltered. A marked thinning of the boundary layer prevents the exponential growth of the vortices because the ratio δ^*/λ_z^* is reduced to a constant, thereby inducing a compression of the three-dimensional spanwise-adjacent structures (Fransson & Alfredsson 2003). The thinning of the boundary layer inhibits the generation of the spanwise and wall-normal pressure gradient and the spanwise viscous diffusion of the disturbances, both instrumental in the growth of the Görtler vortices. Since $\hat{x} = x/Re = O(\delta^2)$ and $\delta \to 0$, the flow tends to be described by the boundary-layer equations, which, for solid walls, apply at locations closer to the leading edge where the pertubations grow at a slower rate (Viaro & Ricco 2019*a*). This slower growth is due to the $\mathcal{Y}$-momentum equation (2.15*c*) not entering the dynamics at leading order in the boundary-layer equations, analogous to the laminar base flow. The curvature effects that are responsible for the inviscid pressure-centrifugal imbalance are therefore negligible.

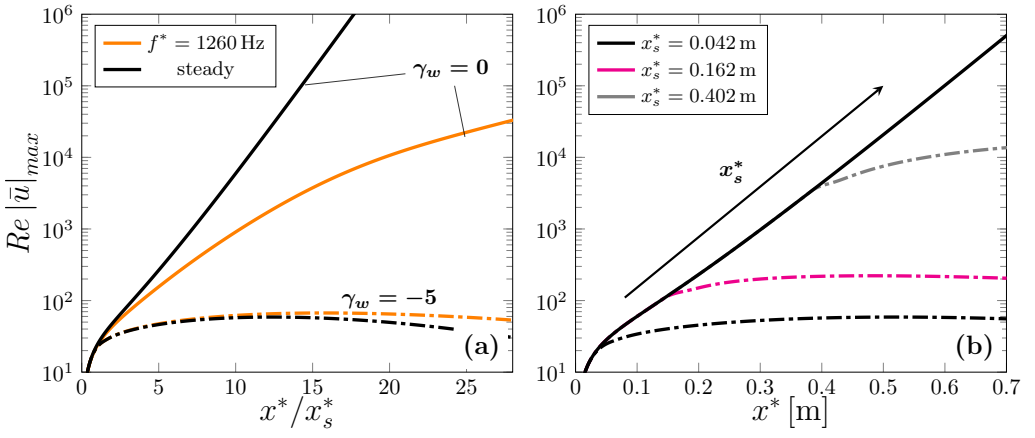

Figure 9: Left (a): effect of γ_w on steady and unsteady Görtler vortices. Right (b): effect of γ_w and x_s^* on steady Görtler vortices. For both graphs, $Ma = 0.8$, $G = 905$ and $Re = 3771$. The pattern of the curves denotes the suction rate $\gamma_w = 0$ (solid) and $\gamma_w = -5$ (dash dot).

The effect of self-similar suction $V(\hat{x}, 0) = V_0/(2\hat{x})^{1/2}$ where $V_0 Re = -5$, is shown in figure 8 (thick curves) and compared with the results of figure 6 (thin curves) for $\gamma_w = -5$ in the subsonic (a) and supersonic (b) cases. In the case of self-similar suction, the boundary-region equations (2.14) reduce to those of Viaro & Ricco (2019*a*). Self-similar suction (thick curves) significantly attenuates the streaks and prevents the onset of the vortices in the subsonic case, thereby damping the disturbance growth right from its inception at the leading edge. The blowing velocity decreases downstream and self-similar suction is outperformed by the uniform suction with $\gamma_w = -5$ and $\lambda_z^* = 1$ mm (magenta curves). An analogous behaviour is reported in the supersonic case (figure 3, b). The curves for the self-similar and non-similar suction cases differ in both shape and amplitude and the results cannot be reconciled by rescaling the plots.

The effect of the free-stream gust frequency on the growth of Görtler vortices under the same conditions of figure 6 is shown in figure 9 (a) ($Ma = 0.80$, $G = 905$, $Re = 3771$ and $x_s^* = 4.2$ cm). A frequency of 1260 Hz is representative of wind-tunnel conditions at moderate Mach numbers (Viaro & Ricco 2019*a*; Xu *et al.* 2024). Uniform suction attenuates steady and unsteady vortices and, when $\gamma_w = -5$, the effect of frequency is negligible. When the boundary layer becomes thinner due to suction, the dynamics is analogous to that near the leading edge. As $\hat{x} \to 0$, the asymptotic behaviour is described by a regular perturbation of the boundary-region equations, expressed as a series summation (Leib *et al.* 1999; Viaro & Ricco 2019*a*). The first terms in this series are governed by the steady boundary-layer equations, which explains the negligible influence of unsteadiness.

The influence of x_s^* on the evolution of the steady vortices is shown in figure 9 (b). The growth rate for $\gamma_w = -2$ does not depend on x_s^*, while the value of maximum streamwise velocity at a given x^* increases with x_s^*. For $\gamma_w = -5$, the disturbance growth is no longer quasi-exponential and settles to an almost constant amplitude for relatively low x_s^*. For the largest tested x_s^*, the boundary layer has grown thicker and the same control is not as effective.

3.3. *Neutral stability curves*

The mathematical formulation presented in §2 incorporates the receptivity of the base flow to free-stream vortical disturbances, allowing a rigorous study of the evolution of the vortices and the plotting of neutral curves for the Görtler instability. The shape of the neutral curves,

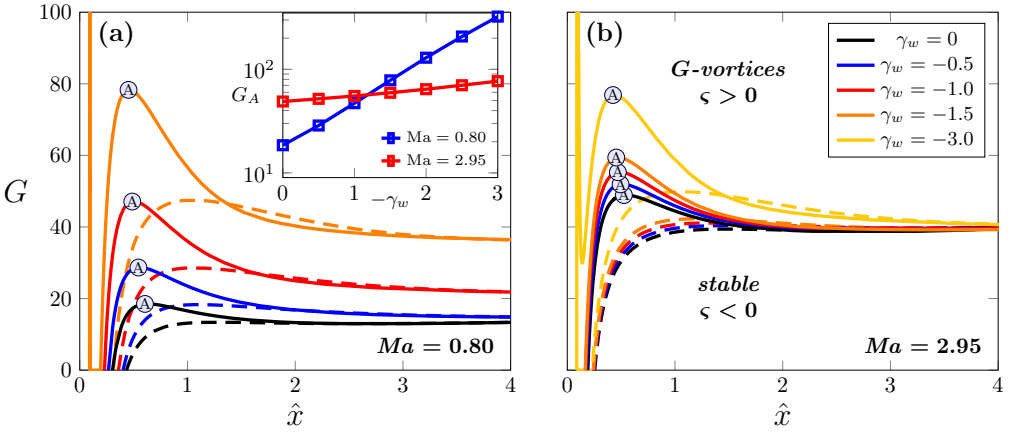

Figure 10: Neutral stability maps of steady ($\mathcal{F} = 0$) Görtler vortices with suction for $k_y = 2$ (solid curves) and $k_y = 1$ (dashed curves) at $Ma = 0.8$ (a) and $Ma = 2.95$ (b) for the conditions of table 1 and $\hat{x}_s = 0.1$. The maximum stable Görtler number G_A is shown as a function of γ_w for $k_y = 2$ in the inset in figure (a).

- i.e. curves in the parameter space that distinguish conditions of growth and decay - is significantly influenced by the initial conditions (Hall 1983), which can only be determined by matching with the outer flow, i.e. by taking receptivity into account. As suggested by Kobayashi (1972), the neutral curves can be easily interpreted if drawn in terms of G (2.16), which only depends on the free-stream conditions and wall curvature, and not on the boundary-layer thickness. We therefore represent the curves as the points of the $\hat{x}$–G parameter space that satisfy the condition $\varsigma(\hat{x}) = 0$, where $\varsigma(\hat{x}) = \mathrm{d}E(\hat{x})/\mathrm{d}\hat{x}$ and

$$E(\hat{x}) = \int_0^\infty |\bar{u}(\hat{x}, \eta)|^2 \, \mathrm{d}\eta \tag{3.9}$$

is the scaled perturbation energy divided by $(2\hat{x})^{1/2}$ (Hall 1983; Viaro & Ricco 2019*b*). The curves in figure 10, drawn for given $\mathcal{F}$, Ma and $\hat{x}_s$, separate stable ($\varsigma < 0$) and unstable ($\varsigma > 0$) regions, with colours denoting the suction rate γ_w. The curves embody the convective nature of Görtler instability: a perturbation evolving in $\hat{x}$ at a fixed G grows in unstable regions and decays in stable regions. The influence of the curvature radius on the Görtler instability when all the other physical parameters are fixed is obtained by changing G at fixed $\hat{x}$ in the maps of figure 10. When r_c is large, G is small, the perturbations evolve as laminar streaks and eventually decay by viscous effects. As r_c decreases, G increases and the laminar streaks become Görtler vortices as they undergo a quasi-exponential growth.

In the subsonic case ($Ma = 0.8$, figure 10, a), the stable region ($\varsigma < 0$) expands considerably and the marked peak near the leading edge becomes more pronounced as γ_w increases. The broadening of the stable region and the reduction in the growth rate caused by increasing suction are similar to those obtained by increasing Ma at constant $\hat{x}$ and Re.

The effect of suction is much weaker in the supersonic case ($Ma = 2.95$, figure 10, b), where the stable region does not broaden as significantly as in the subsonic case, especially downstream of its leading-edge peak. The neutral curves in absence of suction are broader for supersonic Mach numbers because of the stabilising effect of compressibility (Viaro & Ricco 2019*a*). When suction is applied, the suction term in the wall boundary condition (2.12) reduces as T_w increases. The narrow vertical band in figure 10 (a) is due to the transient behaviour shown in the insets of figure 6 (b,d), where suction decreases downstream of $\hat{x}_s$,

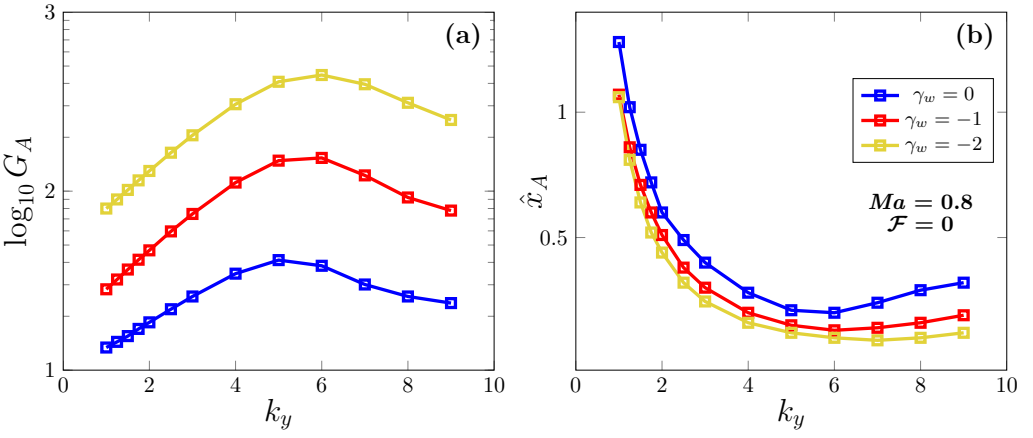

Figure 11: Effect of the wall-normal wavelength of the external disturbance k_y on the maximum stable Görtler number G_A (a) and its location $\hat{x}_A$ (b). The points were computed for increasing suction rates at $Ma = 0.8$.

reaches a minimum, and increases again. As γ_w increases, the stability region broadens upstream and eventually merges with this band (refer to yellow neutral curve in figure 10, b). The maximum stable Görtler number G_A – shown for the peak of the curves with $k_y = 2$ – increases quasi-exponentially with $|\gamma_w|$ (inset in figure 10, a). This change of G_A with $|\gamma_w|$ is more pronounced in the subsonic case. Higher suction rates shift the location where the boundary-layer perturbations become independent of the initial and outer conditions farther downstream.

The importance of receptivity is revealed unequivocally in the influence of the wall-normal wavenumber k_y, a quantity that only enters the problem through the free-stream boundary conditions. The curves for $k_y = 2$ (solid curves in figure 10) show a pronounced peak near the leading edge (letter A) that is almost absent for $k_y = 1$ (dashed). The solid and dashed curves merge at large $\hat{x}$ and the disturbance growth is less impacted by receptivity as the perturbations evolve downstream. The reason for this result resides in the decay of the external perturbations by viscous dissipation, as evident in (2.19). The eigenvalue approach becomes tenable because the external forcing is uninfluential sufficiently downstream (Viaro & Ricco 2019*a*). The highest stable Görtler number G_A and its location on the neutral map $\hat{x}_A$ are sensitive to variations in k_y. G_A increases with k_y when $k_y \leqslant 6$ and decreases for $k_y > 6$ (figure 11, a), while $\hat{x}_A$ moves closer to the leading edge as k_y increases and $k_y \leqslant 6$, but moves slightly downstream for $k_y > 6$ (figure 11, b). The increase of G_A and the decrease of $\hat{x}_A$ observed for $k_y \leqslant 6$ are due to the decaying forcing term in the outer boundary conditions (2.19) and represent the broadening of the stability region in the parameter space $\hat{x} - G$. The presence of moderate wall suction (red curves in figure 11) does not alter the shape of the curves, which shift to higher G_A and smaller $\hat{x}_A$.

The maps in figure 12 show the effect of wall suction on the stability of unsteady Görtler vortices. The shape of the curves is affected by unsteadiness and the stability region expands uniformly for increasing $\mathcal{F}$. For low and moderate disturbance frequency ($\mathcal{F} = 10$, solid curves), the curves expand while retaining the same shape. For larger frequency, the stability region reaches a peak in the vicinity of the leading edge ($\mathcal{F} = 80$, dashed curves) and the neutral curve plateaus downstream, reaching the minimum denoted by the letter B in figure 12. The Görtler number relative to point B decreases abruptly when the disturbance

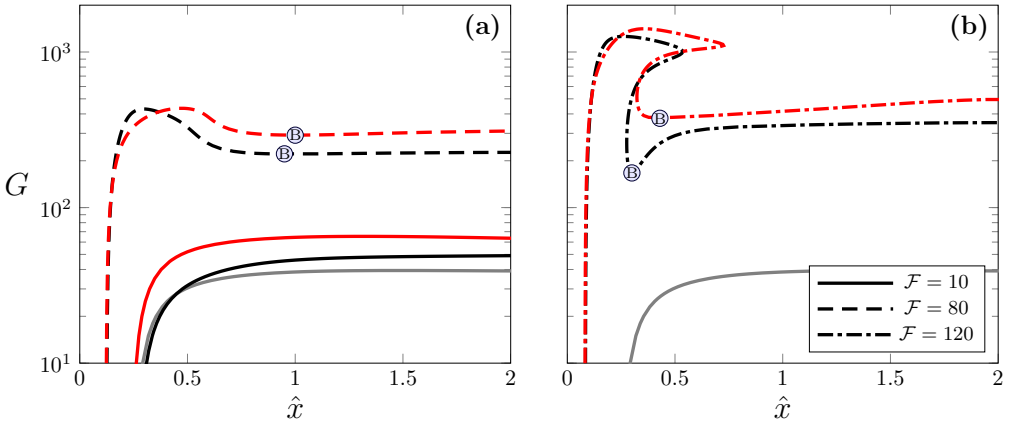

Figure 12: Neutral stability maps of unsteady Görtler vortices for $k_y = 1$ and $Ma = 2.95$. The black and red curves represent the cases $\gamma_w = 0$ and $\gamma_w = -5$, respectively. Left (a): cases $\mathcal{F} = 10$ (solid) and $\mathcal{F} = 80$ (dashed). Right (b): case $\mathcal{F} = 120$. The gray curve shows the steady case without suction ($k_y = 1$, $\mathcal{F} = 0$, $\gamma_w = 0$) for comparison.

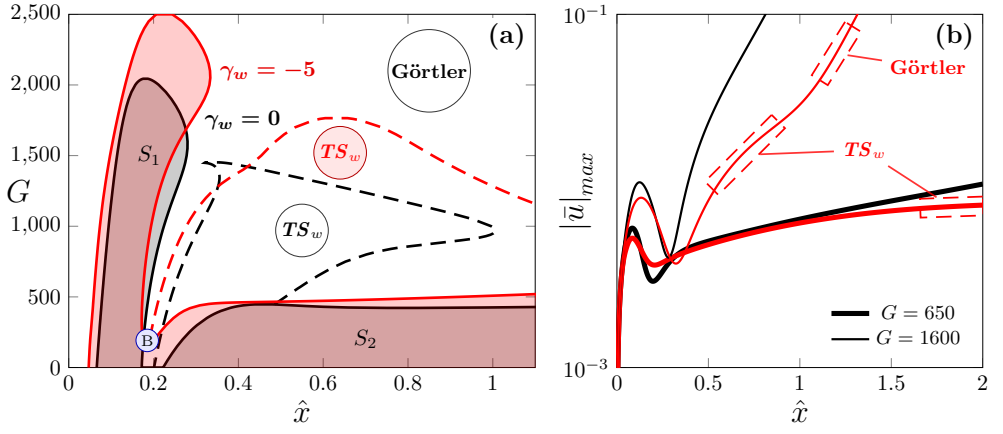

Figure 13: Left (a): neutral maps of Görtler instability (solid curves) at moderate Mach numbers and relatively high disturbance frequency. The stable regions (S_1 and S_2) are enclosed within the solid curves and the regions of weak TS growth (TS_w) within the dashed curves. Right (b): evolution of $|\bar{u}|_{max}$ for $G = 650$ (thick) and $G = 1600$ (thin). For the suction cases, the segments of the curves describing weak (TS) growth and quasi-exponential (Görtler) growth are enclosed in the dashed red rectangles. For both graphs, $Ma = 2.95$, $k_y = 1$, $\mathcal{F} = 150.3$, and $\gamma_w = 0$ (black) and $\gamma_w = -5$ (red).

frequency is increased above $\mathcal{F} > 80$, and a narrow unstable region appears immediately downstream of the leading-edge peak ($\mathcal{F} = 120$, dash-dot curves).

The neutral stability curves of figure 13 (a) show the effect of suction for relatively high disturbance frequency $\mathcal{F}$ in supersonic flows. The shape of this neutral curve for unsteady conditions is markedly different from the map of figure 10 and 12. As $\mathcal{F}$ increases, the peak denoted by the letter A becomes more pronounced, the minimum denoted by B drops dramatically, and the stable region eventually splits in two branches denoted by S_1 and S_2 in 13 (a). The flow experiences three types of instability: laminar streaks, Görtler vortices and oblique TS waves. The latter are generated by a wavelength-shortening mechanism related to

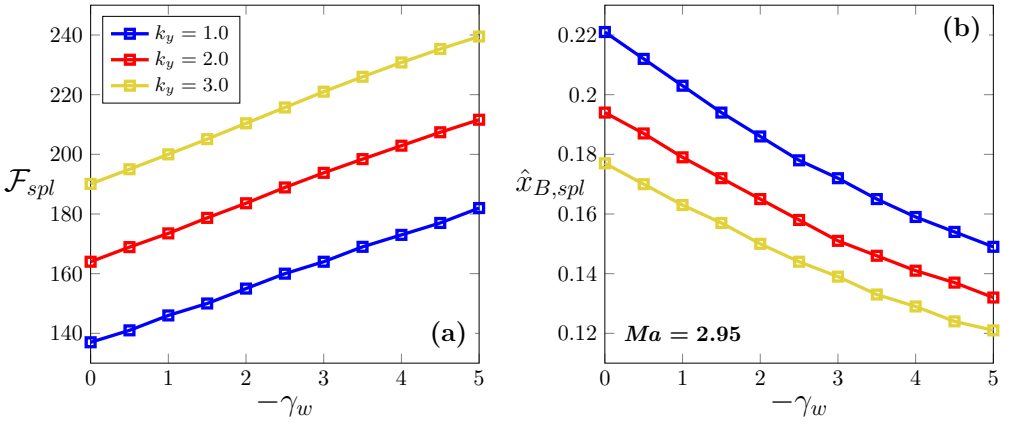

Figure 14: Left (a): splitting frequency $\mathcal{F}_{spl}$ as a function of the suction rate γ_w and the wall-normal wavenumber k_y. Right (b): splitting location at $G = 0$ as a function of γ_w and k_y.

the spanwise pressure gradient of the disturbance, as first shown by Ricco & Wu (2007). For moderate G, the disturbance growth in absence of suction is described by the thick black curve for $G = 650$ in figure 13 (b). Laminar streaks develop upstream of (and attenuate within) S_1. Downstream of S_1, they either decay in S_2 or amplify again as TS waves, their growth being independent of the curvature (Viaro & Ricco 2019*b*). A strong or weak TS growth occurs depending on whether $\beta = \mathrm{d}^2 |\bar{u}|_{max} / \mathrm{d}\hat{x}^2$ is positive or negative, respectively. Regions of $\beta < 0$ are enclosed in the dashed curves in figure 13 (a). Immediately downstream of S_1, β is positive and the TS waves undergo an intense growth ($\beta > 0$). The disturbances then enter the region enclosed by the dashed curve and turn into weak TS waves (white marker TS_w in figure 13 a). Only for very large G the perturbations turn into quasi exponentially-growing Görtler vortices, as shown by the thin black curve for $G = 1600$ in figure 13 (b).

Uniform suction with $\gamma_w = -5$ (red curves in figure 13) broadens the stable regions. The branches S_1 and S_2 merge and all disturbances are attenuated for $G < 150$. Region S_1 broadens almost vertically, while the influence on region S_2 is milder. This finding is consistent with the results for steady conditions at moderate Mach numbers (figure 10, b). The region of the weak TS waves (delimited by the dashed curves in figure 13 a) spreads and covers a large portion of the $\hat{x}$–G plane that would otherwise host the more powerful exponential growth of the strong TS waves or the Görtler vortices (red marker TS_w in figure 13 a). The thick curves for $G = 650$ in figure 13 (b) illustrate the shift from strong to weak ($\beta < 0$) TS growth. When the curvature is more marked (thin curves for $G = 1600$), suction delays the onset of the strong TS waves and the Görtler vortices farther downstream.

With uniform suction at $\gamma_w = -5$, the branches S_1 and S_2 merge again within a narrow band just below point B in figure 12. An increase in disturbance frequency $\mathcal{F}$ lowers point B towards the axis $G = 0$ in the neutral map. As a critical $\mathcal{F}_{spl}$ is attained, the point B reaches $G = 0$ at a streamwise location $\hat{x}_B = \hat{x}_{spl}$. Conversely, increasing the suction rate γ_w has the opposite effect, as it causes S_1 and S_2 to merge and shifts point B to higher Görtler numbers. A higher $\mathcal{F}_{spl}$ is required to split the stable region when suction is applied. As shown in figure 14, $\mathcal{F}_{spl}$ increases linearly with the suction rate γ_w (a), while the streamwise location of the splitting point $\hat{x}_{spl}$ decreases as γ_w increases (b). For the case of the neutral map in figure 13 ($Ma = 2.95$ and $k_y = 1$), the splitting frequency is $\mathcal{F}_{spl} = 137$ in absence of suction (black curve in figure 13 a), but increases to $\mathcal{F}_{spl} = 181$ when a suction rate $\gamma_w = -5$ is applied

(red curve in figure 13 a). As in the subsonic case, a moderate increase in the wall-normal wavenumber k_y has a stabilizing effect on the neutral curves. The lines in figure 14 (a) shift to higher splitting frequencies for $k_y = 2$ (red) and $k_y = 3$ (yellow), while the curves in figure 14 (b) move downwards. This behaviour is consistent with the results reported in figures 10 and 11, which show a rapid upstream shift of the stable peak near the leading edge when k_y increases in the range $1 \leqslant k_y \leqslant 6$.

4. Conclusions

In this study, we have investigated the effect of uniform wall suction on compressible boundary layers evolving over streamwise-concave surfaces and exposed to free-stream vortical disturbances. With the long-term objective of using suction as an effective method for transition delay, we considered suction rates that are achievable across thin porous layers of small permeability and negligible surface roughness.

A laminar boundary layer developing over a suction actuator undergoes a complex evolution from the impermeable leading-edge region to its asymptotic-suction state. We have validated the results of the non-similar laminar base flow with suction against incompressible and supersonic wind-tunnel data and direct numerical simulations. To study the receptivity of the base flow to oncoming free-stream vortical disturbances, we have employed the non-similar compressible boundary-region framework which has been been formulated and solved numerically for the first time. The non-similarity of the viscous layer modifies the asymptotic matching between the external flow and the boundary layer, and thus the free-stream boundary conditions.

Our results demonstrate that wall suction significantly reduces the amplitude of compressible Görtler vortices, expanding the region of stability in the $\hat{x} - G$ parameter space. These findings indicate that suction can be an effective method for controlling the early stages of transition for boundary layers evolving over streamwise-concave surfaces for subsonic and moderately supersonic Mach numbers. The suppression effect weakens as the Mach number (and, therefore, the wall temperature) increases, which suggests that wall suction might not be effective in the hypersonic regime. It may serve nevertheless the purpose of delaying transition in boundary layers evolving over the nozzles of supersonic wind tunnels, thus enhancing their performance, and as a control method for boundary layers over high-speed vehicles. We have computed the neutral stability curves of compressible Görtler vortices with uniform suction, quantifying the enlargement of the stability regions as the suction rate increases.

Future work should focus on extending our formulation to take into account nonlinearity and the secondary instability of the compressible Görtler vortices as next steps to evince the influence of wall suction on transition delay. More complex free-stream forcing conditions or three-dimensional base flows could be considered to obtain a more complete picture of the effect of suction, which cannot be captured by our simplified approach. Suction non-uniformity at the pore scale and the coexistence of acoustic and vortical disturbances should also be studied. The lack of experimental data of suction through concave porous walls in the compressible regime represents a critical issue to be addressed, while future experiments on transitional flows should prioritize velocity field measurements in cross-flow planes to identify where vortical structures first emerge within the boundary layer.

Acknowledgements. LF is grateful to Dr Dongdong Xu, Dr Kaixin Zhu and Dr Matthew Falcone for their comments and support. LF and PR thank the reviewers for their insightful comments that improved the quality of the article.

Funding. The authors acknowledge the financial support of the US Air Force through AFOSR grant FA8655-21-1-7008 (International Program Office - Dr Douglas Smith). The views and conclusions contained herein

are those of the authors and should not be interpreted as necessarily representing the official policies or endorsements, either expressed or implied, of the funding agencies or the US Government. LF was also supported by the University of Sheffield's Postgraduate Research Student Publication Scholarship 2024.

Declaration of interests. The authors report no conflict of interest.

Author ORCIDs. L. Fossà, https://orcid.org/0000-0001-7138-5903; P. Ricco, https://orcid.org/0000-0003-1537-1667

Appendix A. Outer behavior of the base-flow wall-normal velocity

The velocity components of the steady, two-dimensional outer flow in region IV $\{1, 0, 0\} + \epsilon\,\{\acute{u}, \acute{v}, 0\}\,(\hat{x}, \hat{y})$ (2.20) are described by the streamfunction $\Psi\,(\hat{x}, y, \hat{y}) = y + \psi_1\,(\hat{x}, \hat{y})$

$$U_{out} = 1 + \epsilon\,(\acute{\rho} + \acute{u}) = \frac{\partial \Psi}{\partial y} = 1 + \frac{1}{Re}\frac{\partial \psi_1}{\partial \hat{y}}, \tag{A 1a}$$

$$V_{out} = \epsilon \acute{v} = -\frac{1}{Re}\frac{\partial \Psi}{\partial \hat{x}} = -\frac{1}{Re}\frac{\partial \psi_1}{\partial \hat{x}}. \tag{A 1b}$$

Substitution of (2.20) in the Navier-Stokes equations and the perfect gas equation yields the Euler equations for

$$\frac{\partial \acute{u}}{\partial \hat{x}} + \frac{\partial \acute{p}}{\partial \hat{x}} = 0, \tag{A 2a}$$

$$\frac{\partial \acute{v}}{\partial \hat{x}} + \frac{\partial \acute{p}}{\partial \hat{y}} = 0, \tag{A 2b}$$

$$\frac{\partial \acute{\tau}}{\partial \hat{x}} - (\gamma - 1)\,Ma^2 \frac{\partial \acute{p}}{\partial \hat{x}} = 0, \tag{A 2c}$$

$$\gamma Ma^2 \acute{p} - \acute{\rho} - \acute{\tau} = 0. \tag{A 2d}$$

By assuming that shock waves are absent, one can write (A 2*c*) as

$$\frac{\partial \acute{\tau}}{\partial \hat{y}} - (\gamma - 1)\,Ma^2 \frac{\partial \acute{p}}{\partial \hat{y}} = 0, \tag{A 3}$$

and combining (A 3), (A 2*b*), (A 2*d*) and (A 1*b*) yields

$$Ma^2 \frac{\partial^2 \psi}{\partial \hat{x}^2} + r_t \left(\frac{\partial \acute{u}}{\partial \hat{y}} - \frac{\partial \acute{v}}{\partial \hat{x}} \right) = \frac{\partial^2 \psi_1}{\partial \hat{y}^2} + \frac{\partial^2 \psi}{\partial \hat{x}^2}. \tag{A 4}$$

Because the inviscid outer flow is irrotational, the streamfunction ψ_1 is governed by the Poisson equation

$$\left(1 - Ma^2\right) \frac{\partial^2 \psi_1}{\partial \hat{x}^2} + \frac{\partial^2 \psi_1}{\partial \hat{y}^2} = 0. \tag{A 5}$$

Equation (A 5) is solved by matching (A 1*b*) with the large-η limit of the wall-normal velocity component (2.11*b*) given in (2.21). The wall-normal velocity V_{out} decays in the far field for $\hat{y} \gg 1$. The boundary condition at the plate is recovered by matching the inner and outer limits of (A 1*b*) and (2.11*b*), respectively. The streamfunction ψ_1 at $\hat{y} \ll 1$ and $y = O(1)$ is given by (2.23).

In self-similar, compressible boundary layers (2.23) reduces to

$$\psi_1\,(\hat{x}, 0) = -\,(2\hat{x})^{1/2}\,(\gamma_c + \beta_c)\,. \tag{A 6}$$

If the flow is subsonic, equation (A 5) is elliptic and can be solved analytically using complex-

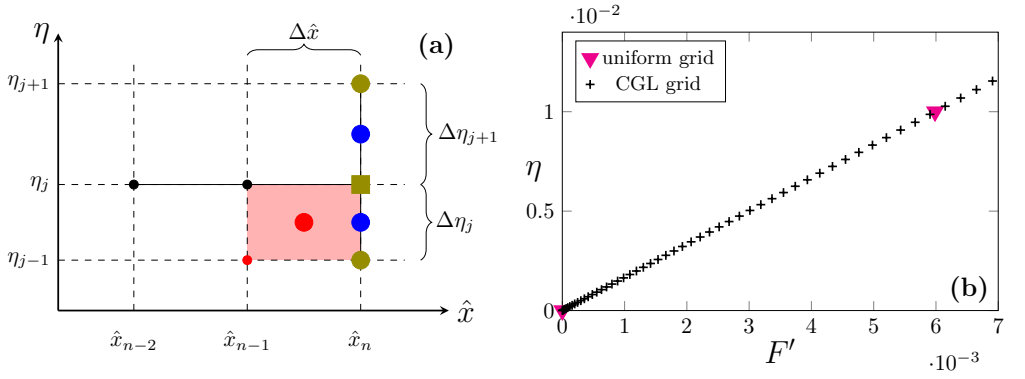

Figure 15: Left (a): schematic of the non-uniform spatial discretization used in the computation of the boundary-region equations. Right (b): base-flow streamwise velocity profile $U = F'$ in the near wall region. A uniform (magenta triangles) and a CGL grid (black crosses) were used to collocate the same number of points $N_p = 3000$ on a width $\eta_{max} = 30$.

variable theory (van Dyke 1975, p. 136)

$$\Psi(x, y) = y - \frac{1}{Re^{1/2}} \mathrm{Re}\left\{\left[2x + 2\mathrm{i}\left(1 - Ma^2\right)^{1/2} y\right]^{1/2} (\beta_c + \gamma_c)\right\}, \tag{A 7}$$

where Re denotes the real part. Equation (A 7) reduces to (5.8) of LWG99 in the incompressible case ($Ma = 0$ and $\gamma_c = 0$).

Appendix B. Numerical solution of the compressible boundary-region equations on non-uniform grids

A schematic of the streamwise and wall-normal grid is shown in figure 15 (a). A Keller-box method is used to compute the base flow. The method is a second-order block-elimination algorithm that computes (2.5) on the staggered grid centred on the red point $(\hat{x}_{n-1/2}, \eta_{j-1/2})$ and uses the variables defined at the vertices of the red rectangle $(\hat{x}_n, \eta_j)$, $(\hat{x}_n, \eta_{j-1})$, $(\hat{x}_{n-1}, \eta_{j-1})$ and $(\hat{x}_{n-1}, \eta_j)$. For further details, the reader is referred to Cebeci (2002).

Once F and T are known, a finite difference scheme is employed to compute the velocity components, $\bar{u}$, $\bar{v}$, $\bar{w}$, the temperature $\bar{\tau}$ and the pressure $\bar{p}$. The terms that multiply $\bar{u}$, $\bar{v}$, $\bar{w}$, $\bar{\tau}$, and $\bar{p}$ are defined at the point $(\hat{x}_n, \eta_j)$ denoted by the olive square. A uniform marching step is used in $\hat{x}$, the streamwise derivatives are estimated by backward differencing and the variables at $(\hat{x}_{n-1}, \eta_j)$ and $(\hat{x}_{n-2}, \eta_j)$ are stored from upstream computations. The wall-normal derivatives are approximated with finite differences schemes centred in $(\hat{x}_n, \eta_j)$

$$\left(\frac{\partial \bar{u}}{\partial \eta}\right)_j = \frac{C_j \bar{u}_{j+1} + \left(1 - C_j\right) \bar{u}_j - \bar{u}_{j-1}}{C_j \Delta\eta_{j+1} + \Delta\eta_j}, \tag{B 1a}$$

$$\left(\frac{\partial^2 \bar{u}}{\partial \eta^2}\right)_j = 2\frac{\mathcal{P}_j \bar{u}_{j+1} - \left(1 + \mathcal{P}_j\right) \bar{u}_j + \bar{u}_{j-1}}{\mathcal{P}_j \Delta\eta_{j+1}^2 + \Delta\eta_j^2}, \tag{B 1b}$$

where the weights are $C_j = (\Delta\eta_j / \Delta\eta_{j+1})^2$ and $\mathcal{P}_j = \Delta\eta_j / \Delta\eta_{j+1}$. Upward finite differences

are used to enforce the adiabatic condition at the wall $j = 1$

$$\left(\frac{\partial \bar{\tau}}{\partial \eta}\right)_1 = \frac{C_{up,1}\bar{\tau}_3 - \bar{\tau}_2 + \left(1 - C_{up,1}\right)\bar{\tau}_1}{C_{up,1}\left(\Delta\eta_3 + \Delta\eta_2\right) - \Delta\eta_2} = 0, \tag{B 2}$$

and $C_{up,1} = \Delta\eta_2^2/(\Delta\eta_3 + \Delta\eta_2)^2$. Downward finite difference schemes are used to enforce the boundary conditions of the mixed type (2.19) at the outer boundary $j = N_p$ - where N_p is the number of points in the wall-normal direction -

$$\left(\frac{\partial \bar{v}}{\partial \eta}\right)_{N_p} = \frac{C_{down,N_p}\bar{v}_{N_p-2} - \bar{v}_{N_p-1} - (C_{down,N_p} - 1)\bar{v}_{N_p}}{\Delta\eta_{N_p} - C_{down,N_p}(\Delta\eta_{N_p} + \Delta\eta_{N_p-1}}, \tag{B 3}$$

where $C_{down,N_p} = \Delta\eta_{N_p}^2/(\Delta\eta_{N_p} + \Delta\eta_{N_p-1})^2$. The asymptotic outer boundary conditions are imposed by introducing

$$\bar{v}_{N_p} = \frac{C_{back,N_p}\bar{v}_{N_p-2} - \bar{v}_{N_p-1} - \mathcal{A}_{N_p} e^{i\mathcal{F}\hat{x} + ik_y(2\hat{x})^{1/2}[\eta - \beta_c(\hat{x})] - \left(k_y^2 + k_z^2\right)\hat{x}}}{C_{back,N_p} - 1 + \mathcal{A}_{N_p}|k_z|(2\hat{x})^{1/2}}, \tag{B 4a}$$

$$\bar{w}_{N_p} = \frac{C_{back,N_p}\bar{w}_{N_p-2} - \bar{w}_{N_p-1}}{C_{back,N_p} - 1 + \mathcal{A}_{N_p}|k_z|(2\hat{x})^{1/2}} + \\ + \frac{\mathcal{A}_{N_p} ik_y (2\hat{x})^{1/2} e^{i\mathcal{F}\hat{x} + ik_y(2\hat{x})^{1/2}[\eta - \beta_c(\hat{x})] - \left(k_y^2 + k_z^2\right)\hat{x}}}{C_{back,N_p} - 1 + \mathcal{A}_{N_p}|k_z|(2\hat{x})^{1/2}}, \tag{B 4b}$$

$$\bar{p}_{N_p} = \frac{C_{back,N_p}\bar{p}_{N_p-2} - \bar{p}_{N_p-1}}{C_{back,N_p} - 1 + \mathcal{A}_{N_p}|k_z|(2\hat{x})^{1/2}}, \tag{B 4c}$$

- where $\mathcal{A}_{N_p} = C_{back,N_p}(\Delta\eta_{N_p} + \Delta\eta_{N_p-1}) - \Delta\eta_{N_p}$ - in the discretization at η_{N_p-1}. The pressure is computed on a staggered grid (blue circles in figure 15) to avoid the odd-even decoupling

$$\bar{p}_{j+1/2} = \frac{\bar{p}_{j+1} + \bar{p}_j}{2}, \tag{B 5}$$

and the wall-normal pressure gradient is

$$\frac{\partial \bar{p}}{\partial \eta} = \frac{\bar{p}_{j+1} - \bar{p}_j}{\Delta\eta_{j+1}}. \tag{B 6}$$

A Chebyshev-Gauss-Lobatto (CGL) grid is used to distribute the grid points (olive points in figure 15, a) in the wall-normal direction (Aref & Balachandar 2018). The location of each point is given by

$$\eta_j = \eta_{max}\left[1 - \cos\left(\frac{\pi j}{2N_p}\right)\right] \text{ for } 0 \leqslant j \leqslant N_p, \tag{B 7}$$

in the range $\eta \in [0, \eta_{max}]$. The base-flow results obtained on uniform and CGL grids with $N_p = 3000$ and $\eta_{max} = 30$ are compared in figure 15 (b). The CGL grid (black crosses) is substantially more refined than the uniform grid (magenta triangles) in the near-wall region. Grid independence in η was verified by increasing $\eta_{\max}$ to 60 and N_p to 6000. Grid independence in $\hat{x}$ was ensured by repeating the computations with different marching steps: $\Delta\hat{x} = 10^{-3}$, 5×10^{-4}, 10^{-4}, and 5×10^{-5}. We adopted $\Delta\hat{x} = 10^{-4}$ for the computations presented in this paper.

To validate the algorithm and the use of the CGL grid, we followed Wu *et al.* (2011),

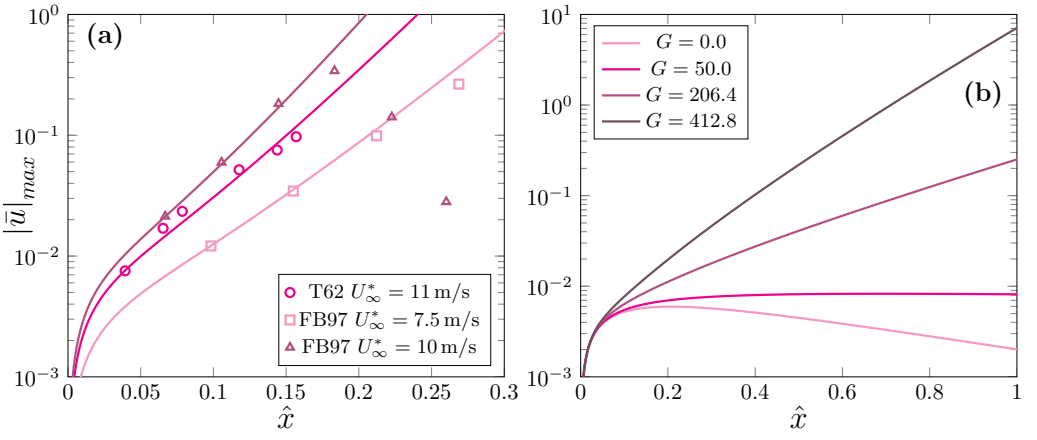

Figure 16: Validation of the disturbance flow without suction computed on the CGL grid. Left (a): the growth of the steady, incompressible Görtler vortices compared against the experimental data of Tani (1962, T62) and Finnis & Brown (1997, FB97) as in Wu *et al.* (2011). Right (b): the growth of compressible steady Görtler vortices compares well with the results of (Viaro & Ricco 2019*a*, fig. 9a) for $Ma = 4.0$ and $k_y = 1$.

and compared our solution to (2.15*a*)–(2.15*e*) - which reduce to the form of Viaro & Ricco (2019*a*) in absence of suction - against the incompressible wind tunnel data of Tani (1962, T62) and Finnis & Brown (1997, FB97). Since the amplitude of the free-stream gusts ϵ was not provided in T62 or in FB97, the numerical results were rescaled with respect to the experimental data point located furthest upstream (Xu *et al.* 2017). The agreement is good for all the cases (refer to figure 16). Unfortunately, a direct comparison with the supersonic wind tunnel data of Wang *et al.* (2018) is not possible and an experimental validation cannot be performed in the compressible regime. As shown in figure 16 (b), our code reproduces the computations of Viaro & Ricco (2019*a*) (figure 9a therein) for the case $Ma = 4.0$ and $k_y = 1$ and different Görtler numbers.

Finally, the discrete points of the neutral stability curves in §3.3 were computed by solving the CLUBR equations for increasing G and storing the streamwise location of the neutral point. In most cases, the neutral curves are functions $G_\varsigma\,(\hat{x})$, where G_ς is the Görtler number corrisponding to a neutral point, and a Quicksort algorithm (Hoare 1962) was used to sort the detected points for ascending $\hat{x}$.

REFERENCES

Al-Malki, M., Hussain, Z., Garrett, S. & Calabretto, S. 2021 Effects of parietal suction and injection on the stability of the Blasius boundary-layer flow over a permeable, heated plate. *Phys. Rev. Fluids* **6**, 113902.

Anderson, J. D. 2016 *Fundamentals of aerodynamics*. McGraw-Hill Education.

Anderson, J. D. 2019 *Hypersonic and high-temperature gas dynamics*. AIAA.

Aref, H. & Balachandar, S. 2018 *A first course in computational fluid dynamics*. Cambridge University Press.

Beckwith, I. E. & Bertram, M. H. 1972 A survey of NASA Langley studies on high-speed transition and the quiet tunnel. *Tech. Memo.* NASA-TM-X-2566. NASA Langley Res. Cent.

Beckwith, I. E., Harvey, W. D., Harris, J. E. & Holley, B. B. 1973 Control of supersonic wind-tunnel noise by laminarization of nozzle-wall boundary layer. *Tech. Rep.* NASA-TM-X-2879. NASA Langley Res. Cent.

Bountin, D. A., Gromyko, Y. V., Maslov, A. A., Polivanov, P. A. & Sidorenko, A. A. 2016 Effect of the surface roughness of blunt cone forebody on the position of laminar-turbulent transition. *Thermophys. Aeromech.* **23** (5), 629–638.

Cebeci, T. 2002 *Convective Heat Transfer*. Horizons Publ.

Ciolkosz, L. D. & Spina, E. F. 2006 An experimental study of Görtler vortices in compressible flow. In *42nd AIAA/ASME/SAE/ASEE Jt. Propuls. Conf.*, *AIAA Paper* 2006-4512. AIAA.

Dimond, B., Costantini, M. & Klein, C. 2022 Experimental analysis of the effect of suction and step height on boundary-layer transition. In *IUTAM Laminar-Turbul. Transit.* (ed. S. Sherwin, P. Schmid & X. Wu), pp. 171–180. Cham: Springer Int. Publ.

Dimond, B., Costantini, M., Risius, S., Klein, C. & Rein, M. 2020 Experimental investigation of the delay of gap- and step-induced transition by means of suction. In *New Results Numer. Exp. Fluid Mech. XII*, pp. 165–174. Cham: Springer Int. Publ.

van Dyke, M. 1975 *Perturbation methods in fluid mechanics*. Stanford: Parabolic Press.

El-Hady, N. M. & Verma, A. K. 1981 Growth of Görtler vortices in compressible boundary layers along curves surfaces. In *14th Fluid Plasma Dyn. Conf.*, *AIAA Paper* 1981-1278. AIAA.

El-Hady, N. M. & Verma, A. K. 1984 Instability of compressible boundary layers along curved walls with suction or cooling. *AIAA J.* **22** (2), 206–213.

Es-Sahli, O., Sescu, A., Koshuriyan, M. Z. A., Hattori, Y. & Hirota, M. 2023 Lagrange multiplier-based optimal control technique for streak attenuation in high-speed boundary layers. *AIAA J.* **61** (1), 63–75.

Finnis, M. V. & Brown, A. 1997 The linear growth of Görtler vortices. *Int. J. Heat Fluid Flow* **18** (4), 389–399.

Flechner, S. G., Jacobs, P. F. & Whitcomb, R. T. 1976 A high subsonic speed wind tunnel investigation of winglets on a representative second-generation jet transport wing. *Tech. Rep.* NASA-TN-D-8264. NASA Langley Res. Cent.

Floryan, J. M. 1997 Stability of wall-bounded shear layers in the presence of simulated distributed surface roughness. *J. Fluid Mech.* **335**, 29–55.

Floryan, J. M. & Saric, W. S. 1979 Stability of Görtler vortices in boundary layers with suction. In *12th Fluid Plasma Dyn. Conf.*, *AIAA Paper* 1979-1497.

Floryan, J. M. & Saric, W. S. 1983 Effects of suction on the Görtler instability of boundary layers. *AIAA J.* **21** (12), 1635–1639.

Fransson, J. H. M. & Alfredsson, P. H. 2003 On the disturbance growth in an asymptotic suction boundary layer. *J. Fluid Mech.* **482**, 51–90.

Goldstein, M. E. 1983 The evolution of Tollmien–Schlichting waves near a leading edge. *J. Fluid Mech.* **127**, 59–81.

Görtler, H. 1957 On the calculation of steady laminar boundary layer flows with continuous suction. *J. Math. Mech.* **6** (3), 323–340.

Graziosi, P. & Brown, G. L. 2002 Experiments on stability and transition at Mach 3. *J. Fluid Mech.* **472**, 83–124.

Griffith, A. A. & Meredith, F. W. 1936 The possible improvement in aircraft performance due to the use of boundary-layer suction. *Tech. Rep.* 2315 RAE E 3501. Aeronaut. Res. Counc.

Gui, Y., Zhang, C., Li, X., Xu, D. & Wu, J. 2023 Hypersonic boundary-layer instability characterization and transition downstream of distributed roughness. *Exp. Fluids* **64** (10), 159.

Hader, C. & Fasel, H. F. 2021 Flow control using steady blowing and suction strips in a Mach 6 boundary layer on a flared cone. In *AIAA Scitech 2021 Forum*, *AIAA Paper* 2021-1206.

Hall, P. 1983 The linear development of Görtler vortices in growing boundary layers. *J. Fluid Mech.* **130**, 41–58.

Hoare, C. A. R. 1962 Quicksort. *Comput. J.* **5** (1), 10–16.

Hollender, C., Dwivedi, A. & Candler, G. V. 2019 Response of a Mach 6 cone-flare geometry to steady vortical disturbances: Effect of steady suction. In *AIAA Aviat. 2019 Forum*, *AIAA Paper* 2019-3219.

Kay, J. M. 1953 Boundary-layer flow along a flat plate with uniform suction. ARC Tech. Rep. 2628. Camb. Univ. Eng. Lab.

Kobayashi, R. 1972 Note on the stability of a boundary layer on a concave wall with suction. *J. Fluid Mech.* **52** (2), 269–272.

Kobayashi, R. 1974 Taylor-Görtler instability of a boundary layer with suction or blowing. *AIAA J.* **12** (3), 394–395.

Krishnan, K. S. G., Bertram, O. & Seibel, O. 2017 Review of hybrid laminar flow control systems. *Prog. Aerosp. Sci.* **93**, 24–52.

Kurian, T. & Fransson, J. H. M. 2011 Transient growth in the asymptotic suction boundary layer. *Exp. Fluids* **51** (3), 771–784.

Leib, S. J., Wundrow, D. W. & Goldstein, M. E. 1999 Effect of free-stream turbulence and other vortical disturbances on a laminar boundary layer. *J. Fluid Mech.* **380**, 169–203.

Leontiev, A. I. & Pavlyuchenko, A. M. 2008 Investigation of laminar-turbulent transition in supersonic boundary layers in an axisymmetric aerophysical flight complex and in a model in a wind tunnel in the presence of heat transfer and suction of air. *High Temp.* **46** (4), 542–565.

Lew, H. G. & Fanucci, J. B. 1955 On the laminar compressible boundary layer over a flat plate with suction or injection. *J. Aeronaut. Sci.* **22** (9), 589–597.

Li, F., Choudhari, M. M., Paredes, P., Schneider, S. P. & Portoni, P. 2018 Görtler instability and its control via surface suction over an axisymmetric cone at Mach 6. In *2018 Fluid Dyn. Conf.*, *AIAA Paper* 2018-3069. AIAA.

de Luca, L., Cardone, G., Aymer de la Chevalerie, D. & Fonteneau, A. 1993 Goertler instability of a hypersonic boundary layer. *Exp. Fluids* **16** (1), 10–16.

Mangalam, S., Dagenhart, J. & Kalburgi, V. 1987 Influence of suction and curvature on the growth of Görtler vortices on an airfoil. In *25th AIAA Aerosp. Sci. Meet.*, *AIAA Paper* 1987-0481. AIAA.

Marensi, E. & Ricco, P. 2017 Growth and wall-transpiration control of nonlinear unsteady Görtler vortices forced by free-stream vortical disturbances. *Phys. Fluids* **29** (11), 114106.

Maslov, A. A., Shiplyuk, A. N., Sidorenko, A. A. & Arnal, D. 2001 Leading-edge receptivity of a hypersonic boundary layer on a flat plate. *J. Fluid Mech.* **426**, 73–94.

Matsubara, M. & Alfredsson, P. H. 2001 Disturbance growth in boundary layers subjected to free-stream turbulence. *J. Fluid Mech.* **430**, 149–168.

Messing, R. & Kloker, M. J. 2010 Investigation of suction for laminar flow control of three-dimensional boundary layers. *J. Fluid Mech.* **658**, 117–147.

Methel, J., Forte, M., Vermeersch, O. & Casalis, G. 2021 Experimental investigation on the effect of forward-facing steps and gaps combined with wall suction on boundary layer transition. *Exp. Fluids* **63** (1), 21.

Morduchow, M. 1963 General asymptotic solution of the laminar compressible boundary layer with heat transfer. *AIAA J.* **1** (8), 1949–1951.

Myose, R. Y. & Blackwelder, R. F. 1995 Control of streamwise vortices using selective suction. *AIAA J.* **33** (6), 1076–1080.

Negi, P. S., Mishra, M. & Skote, M. 2015 DNS of a single low-speed streak subject to spanwise wall oscillations. *Flow Turbul. Combust.* **94** (4), 795–816.

Panday, S. & Floryan, J.M. 2023 Accurate determination of stability characteristics of spatially modulated shear layers. *J. Fluid Mech.* **975**, A50.

Polyanin, A. D. & Nazaikinskii, V. E. 2015 *Handbook of Linear Partial Differential Equations for Engineers and Scientists*, 2nd edn. CRC Press.

Ricco, P. & Dilib, F. 2010 The influence of wall suction and blowing on boundary-layer laminar streaks generated by free-stream vortical disturbances. *Phys. Fluids* **22** (4), 044101.

Ricco, P., Shah, D. & Hicks, P. D. 2013 Compressible laminar streaks with wall suction. *Phys. Fluids* **25** (5), 054110.

Ricco, P. & Wu, X. 2007 Response of a compressible laminar boundary layer to free-stream vortical disturbances. *J. Fluid Mech.* **587**, 97–138.

Roberts, P. J. D. & Floryan, J. M. 2002 Instability of accelerated boundary layers induced by surface suction. *AIAA J.* **40** (5), 851–859.

Roberts, P. J. D. & Floryan, J. M. 2008 Instability of adverse-pressure-gradient boundary layers with suction. *AIAA J.* **46** (10), 2416–2423.

Roberts, P. J. D., Floryan, J. M., Casalis, G. & Arnal, D. 2001 Boundary layer instability induced by surface suction. *Phys. Fluids* **13** (9), 2543–2552.

Running, C. L., Bemis, B. L., Hill, J. L., Borg, M. P., Redmond, J. J., Jantze, K. & Scalo, C. 2023 Attenuation of hypersonic second-mode boundary-layer instability with an ultrasonically absorptive silicon-carbide foam. *Exp. Fluids* **64** (4), 79.

Saric, W. S. 1985 Laminar flow control with suction: theory and experiment. *AGARD Rep.* **723**.

Schmidt, B. E., Bitter, N. P., Hornung, H. G. & Shepherd, J. E. 2016 Injection into supersonic boundary layers. *AIAA J.* **54** (1), 161–173.

Schneider, Steven P. 2008*a* Development of hypersonic quiet tunnels. *J. Spacecr. Rockets* **45** (4), 641–664.

Schneider, S. P. 2008*b* Effects of roughness on hypersonic boundary-layer transition. *J. Spacecr. Rockets* **45** (2), 193–209.

Sescu, A., Alaziz, R. & Afsar, M. 2018 Control of Görtler vortices in high-speed boundary layers. In *2018 AIAA Aerosp. Sci. Meet.*, *AIAA Paper* 2018-1078.

Sescu, A., Alaziz, R. & Afsar, M. 2019 Effect of wall transpiration and heat transfer on Görtler vortices in high-speed flows. *AIAA J.* **57** (3), 1159–1171.

Sims, J. L. 1964 Tables for supersonic flow around right circular cones at zero angle of attack. *Tech. Rep.* NASA-SP-3004. NASA Marshall Space Flight Center, NASA Special Publication.

Stewartson, K. 1964 *The theory of laminar boundary layers in compressible fluids*. Clarendon Press.

Swearingen, J. D. & Blackwelder, R. F. 1987 The growth and breakdown of streamwise vortices in the presence of a wall. *J. Fluid Mech.* **182**, 255–290.

Tandiono, T., Winoto, S. H. & Shah, D. A. 2008 On the linear and nonlinear development of Görtler vortices. *Phys. Fluids* **20** (9), 094103.

Tani, I. 1962 Production of longitudinal vortices in the boundary layer along a concave wall. *J. Geophys. Res.* **67** (8), 3075–3080.

Traub, H., Kube, J., Jose, S., Prasannakumar, A. & Hühne, C. 2024 Structural and aerodynamic characteristics of micro-perforated porous sheets for laminar flow control. In *ASME 2024 Aerosp. Struct. Struct. Dyn. Mater. Conf.*, *Proc. ASME 2024* SSDM2024-121620, p. V001T03A020.

Viaro, S. & Ricco, P. 2019*a* Compressible unsteady Görtler vortices subject to free-stream vortical disturbances. *J. Fluid Mech.* **867**, 250–299.

Viaro, S. & Ricco, P. 2019*b* Neutral stability curves of compressible Görtler flow generated by low-frequency free-stream vortical disturbances. *J. Fluid Mech.* **876**, 1146–1157.

Wang, Q., Wang, Z. & Zhao, Y. 2018 Visualization of Görtler vortices in supersonic concave boundary layer. *J. Vis.* **21** (1), 57–62.

Wedin, H., Cherubini, S. & Bottaro, A. 2015 Effect of plate permeability on nonlinear stability of the asymptotic suction boundary layer. *Phys. Rev. E* **92**, 013022.

Wu, X., Zhao, D. & Luo, J. 2011 Excitation of steady and unsteady Görtler vortices by free-stream vortical disturbances. *J. Fluid Mech.* **682**, 66–100.

Wundrow, D. W. & Goldstein, M. E. 2001 Effect on a laminar boundary layer of small-amplitude streamwise vorticity in the upstream flow. *J. Fluid Mech.* **426**, 229–262.

Xu, D., Liu, J. & Wu, X. 2020 Görtler vortices and streaks in boundary layer subject to pressure gradient: excitation by free stream vortical disturbances, nonlinear evolution and secondary instability. *J. Fluid Mech.* **900**, A15.

Xu, D., Ricco, P. & Duan, L. 2024 Görtler instability and transition in compressible flows. *AIAA J.* **62** (2), 489–517.

Xu, D., Zhang, Y. & Wu, X. 2017 Nonlinear evolution and secondary instability of steady and unsteady Görtler vortices induced by free-stream vortical disturbances. *J. Fluid Mech.* **829**, 681–730.

Yang, G. & Weigand, B. 2018 Investigation of the Klinkenberg effect in a micro/nanoporous medium by direct simulation Monte Carlo method. *Phys. Rev. Fluids* **3**, 044201.

Yoshioka, S., Fransson, J. H. M. & Alfredsson, P. H. 2004 Free stream turbulence induced disturbances in boundary layers with wall suction. *Phys. Fluids* **16** (10), 3530–3539.

Young, A. D. 1948 Note on the velocity and temperature distributions attained with suction on a flat plate of infinite extent in compressible flow. *Quart. J. Mech. Appl. Math.* **1** (1), 70–75.